NOTE TO USERS

This reproduction is the best copy available.

UMI®

Modeling Curvilinear Flows in Hydraulic Structures

Rahim Tadayon

A Thesis

In the Department

of

Building, Civil and Environmental Engineering

Presented in Partial Fulfillment of the Requirements
For the Degree of Doctor of Philosophy at
Concordia University
Montreal, Quebec, Canada

March 2009

Canada

ABSTRACT

Modeling Curvilinear Flows in Hydraulic Structures

Rahim Tadayon, Ph.D.
Concordia University, 2009

The Study investigates the use of Computational Fluid Dynamics (CFD) to analyze the mean characteristics of curvilinear flows in selected hydraulic structures. Three chosen turbulence models are associated with the Volume of Fluid (VOF) scheme to predict the characteristics of the mean flow. Many hydraulic structures in engineering practice involve highly curvilinear flows. Five typical hydraulic structures commonly used for flow regulation or flow measurement are considered in the present study; cut-throat flumes, lateral weirs, sharp-crested weirs, circular spillways, and siphon spillways. Velocity distributions, pressure distributions, water surface profiles, secondary flows, and discharge coefficients are the mean characteristics of flows that are studied.

Presently, computing methods and high speed computers are strong tools for engineers. With the help of a properly validated numerical model, one can avoid the time consuming and expensive experimental tests based on the physical models to obtain the characteristics of highly curvilinear flows encountered in hydraulic practices. This is based on the fact that unlike physical models, it is far simpler to apply changing boundary conditions and flow parameters to a solved numerical model and obtain a flow characteristics for hydraulic structures associated with highly curvilinear flows.

The flows in hydraulic structures are turbulent. Hence, one needs to solve numerically the continuity equation and momentum equations, including turbulent stresses, as the

governing equations of turbulent flows. Because the above mentioned flows are generally complex and highly curvilinear, the transport equations are needed to model the turbulent stresses in the momentum equations.

In the present study, three Reynolds-Averaged Navier-Stokes (RANS) schemes are used to simulate the turbulent flows. Specifically, the Reynolds stress model (RSM), the Standard k-ε model, and the RNG k-ε model were used in the present study. Further, the VOF scheme is adopted to find the shape of free surface profiles.

ACKNOWLEDGEMENTS

Table of Contents

List of Figures

List of Tables

Notations and Abbreviations

I. Common Notations

C = Dimensionless constant = 5.45;

c = Void fraction;

D_h = Hydraulic diameter (= $4R_h$);

g = Gravitational acceleration;

k = Turbulent kinetic energy (= $\tau_{ii}/2$);

p = Pressure;

$\tilde{p}$ = Instantaneous pressure;

Q = Discharge;

R_h = Hydraulic radius;

S_{ij} = Strain-rate tensor;

$\tilde{S}_{ij}$ = Strain-rate tensor (for instantaneous velocity components);

t = Time;

$\vec{U}$ = Velocity vector;

u_j = Average flow velocity (j = 1, 2, 3);

u_τ = Friction velocity;

$\tilde{u}$ = Instantaneous velocity;

u' = Fluctuating part of velocity;

u = Mean velocity component parallel to solid surface;

v = Mean velocity component perpendicular to solid surface;

x, y, z = Local coordinates; tangent and normal to the solid surface and normal to the x-y plane, respectively;

x_j = Global Cartesian coordinate (j = 1, 2, 3);

Γ = Diffusion coefficient;

γ = Specific weight;

δ_{ij} = Kronecker symbol (δ_{ij} = 1 if i = j and δ_{ij} = 0 otherwise);

ε = Dissipation rate of turbulent kinetic energy;

κ = von Karman's constant = 0.42;

μ = Dynamic viscosity;

v = Kinematic viscosity;

v_T = Kinematic eddy viscosity;

ρ = Density;

$\sigma_k, \sigma_\varepsilon$ = Dimensionless constants;

τ_{ij} = Reynolds-stress tensor;

τ_w = Surface shear stress;

ϕ = General property of fluid;

ϕ_a = General property of air;

ϕ_w = General property of water;

II. Notations (Cut-throat Flumes)

B = Width of channel;

B_T = Width of throat;

h_0 = Pressure head at *2-2* (Fig. 3.1), $x_1 = 0$;

h_N = Non-dimensional h_0 $\left(= \dfrac{h_0}{B_T}\right)$;

L = Length of cut-throat flume;

Q_N = Non-dimensional Q $\left(= \dfrac{Q}{\sqrt{g}\, B_T\, h_0^{1.5}}\right)$;

III. Notations (Side Weirs)

B = Width of channel;

C_m = Discharge coefficient of side weir;

d_0 = Depth of flow upstream of weir;

F_{r1} = Froude number of flow upstream of weir;

L = Length of weir;

L_{1-2} = Total length of channel;

Q_s = Discharge of side weir;

q_s = Discharge of side weir per unit length;

s = Height of weir crest from the channel bed;

IV. Notations (Sharp-Crested Weirs)

C_d = Weir discharge coefficient;

Fr_a = Froude number for the approach flow;

H_1 = Water head upstream of weir measured from the crest level;

w = Weir height;

q = Discharge of approach flow per unit width;

U_0 = Reference velocity $= \sqrt{2gH_1}$;

U_c = Average horizontal velocity at the weir crest section;

x = Axial distance from c (Fig. 5.1) along channel wall;

Y = Normal distance from the wall;

Y_a = Water depth in the approach channel;

Y_c = Flow depth at section c-c (Fig. 5.1);

Y_0 = Flow depth at section s-s (Fig. 5.1);

y = Vertical distance from c (Fig. 5.1) perpendicular to channel wall (floor);

ϕ = Angle of the velocity vector with the horizontal (= $\tan^{-1} v/u$);

V. Notations (Siphon Spillways)

C_d = Discharge coefficient;

d = Siphon throat depth;

H_1 = Total head of water, upstream reservoir, measured from d/s channel bottom;

h_1 = Total head of water, upstream reservoir, measured from crest level;

H_2 = Total head of water, tailwater, measured from d/s channel bottom;

q = Discharge per unit width;

R_1 = Radius of crest;

R_2 = Radius of crown;

TEL = Total Energy Line;

$\Delta H = H_1 - H_2$;

VI. Notations (Circular Spillways)

C_d = Discharge coefficient;

H_1 = Total head reckoned above crest level;

L_a = Length of approach channel;

q = Discharge per unit width;

R = Radius of circular spillway crest;

TEL = Total Energy Line;

w = Spillway height;

α = Upstream slope angle;

β = Downstream slope angle;

VII. Abbreviations

2D   Two-dimensional;

3D   Three-dimensional;

CDS   Central Difference Scheme;

CFD   Computational Fluid Dynamics;

CV   Control Volume;

DNS   Direct Numerical Simulation;

FVM   Finite Volume Method;

LDV   Laser Doppler Velocimetry;

LES   Large Eddy Simulation;

PISO   Pressure Implicit with Splitting of Operations;

UDS   Upwind Difference Scheme;

RANS   Reynolds-Averaged Navier-Stokes;

RSM   Reynolds Stress Model;

RNG   Renormalization Group;

SIMPLE   Semi-Implicit Method for Pressure-Linked Equations;

SIMPLEC   SIMPLE-Consistent;

SIMPLER SIMPLE Revised;

VOF   Volume Of Fluid;

.

CHAPTER 1

INTRODUCTION

1.1 General Remarks

Many hydraulic structures in engineering practice involve highly curvilinear flows. Among these hydraulic structures, those used for flow regulation and flow measurement are most commonly encountered units. Cut-throat flumes and sharp-crested weirs commonly serve as the simple flow-measuring devices in open channels in water and wastewater works. Side weirs can be announced to be the simplest flow regulation for open channels in irrigation systems. Circular spillways and weirs can be selected as uncomplicated devices to regulate the water level in storage systems and diversion works. When a high rate of water is needed to discharge with narrow limits of headwater rise in a reservoir, a siphon spillway could be a good choice.

Computing methods and high speed computers are strong tools for engineers, nowadays. Therefore, one does not need to perform time consuming and expensive experimental test procedures to obtain the mean characteristics of flows in hydraulic practices. Numerical methods (Computational Fluid Dynamics, CFD) with their advantages of lower cost and greater flexibility can reasonably predict the mean characteristics of flows such as velocity distributions, pressure distributions, and water surface profiles of complex problems in hydraulic engineering.

The flows in the above hydraulic structures are turbulent. Hence, one needs to solve numerically the continuity equation and the momentum equations, including turbulent stresses, as the governing equations of turbulent flows. Because these flows are generally

complex and highly curvilinear, transport equations are needed to model the turbulent stresses in the momentum equations, based on accurate turbulence models.

Momentum equations and transport equations of turbulence are higher-order partial differential equations with nonlinear terms. Consequently, one cannot solve them analytically to find a general solution. Therefore, a numerical solution is a key. To use a numerical solution, a numerical discretization technique such as finite element method, finite difference method, or finite volume method is needed to convert the partial differential equations to the algebraic equations. Although the above three techniques or other methods have been used by investigators, finite volume method (FVM) is preferred in CFD field. To capture the shape of the free water surface, a technique such as the Volume Of Fluid (VOF) scheme is needed to be solved along with the governing equations and the turbulent transport equations.

The most accurate approach to turbulence simulation is the direct numerical simulation (DNS) method in which the Navier-stokes equations (continuity and momentum equations) are solved for all spatial and time scales of motions in the three-dimensional domain. From the conceptual aspect, it is the simplest method. On the other hand, the number of grid points, which is needed to capture all scales of motions, is limited by the computing speed and the computer memory. Thus, this method is applicable only for flows in geometrically simple domains and at relatively low Reynolds number. Also, the results of the DNS contain very detailed information about the flow that has far more information than any engineer needs. Further, it is too expensive to be employed very often and cannot be used as a design tool (Ferziger and Peric, 2002).

The second most accurate method is the Large Eddy Simulation (LES) in which the small eddies are modeled and the large eddies (large-scale motions) that are generally much more energetic than the small ones are solved. The time and storage demands for LES are less than those for DNS. However, large eddy simulations are time dependent and still need high-speed computers that make them expensive even though less costly than DNS for the same problem.

When one needs to obtain a few quantitative properties of a turbulent flow, the simpler models such as Reynolds-Averaged Navier-Stokes (RANS) models can be used. These are less expensive than DNS and LES. Instead of solving all motions by DNS or large-scale motions by LES of a turbulent flow, a RANS model can provide the mean characteristics of the flow. The most accurate RANS model is the Reynolds stress model (RSM) in which the turbulent stresses and consequently anisotropic turbulent quantities are solved. The isotropic turbulence models are based on the Boussinesq approximation. Hence, the turbulent stresses are not solved but are modeled. Thus, they are less time consuming than RSM. Among the isotropic turbulence models, the two-equation models (such as the k-ε and the k-ω models) are the simplest complete RANS models.

1.2 Research Objectives

The main objective of this study is to numerically simulate the curvilinear flows in several common hydraulic structures using turbulence modeling. The RANS equations along with turbulence transport equations are modeled using three turbulence models (Standard k-ε model, RNG k-ε model, and RSM). The Volume Of Fluid (VOF) technique is adopted to find the free surface profiles in the structures. The finite volume

method (FVM) as a discretization technique is used to convert the partial differential equations to the algebraic equations.

The mean flow characteristics including water surface profiles, pressure distributions, velocity distributions, secondary flows, and discharge coefficients are obtained. To validate the numerical predictions, experimental results are used. The experimental data include existing results and results based on the present studies.

- Three-dimensional flows resulting in cut-throat flumes are simulated using RSM. Pressure distributions, velocity distributions, water surface profiles, and secondary flows are obtained. Two sets of the previous experimental data as well as the results of a new test are used to validate the numerical predictions.

- Side weir flows are modeled using the three-dimensional RSM. Velocity distributions, water surface profiles, and flow rates over the side weir are predicted. Two sets of previous experimental results are used to validate numerical predictions.

- Two-dimensional RNG k- ε model is used to calculate the velocity and pressure distributions as well as the water surface profiles of flows over the sharp-crested weirs. Two sets of the previous experimental data are used to validate the model predictions.

- Flows through the siphon spillways are modeled using RSM to predict the coefficient of discharge. The data obtained from a test on a siphon model set up in the laboratory is used to evaluate the predicted results by the numerical

simulations. Also, an existing set of experimental data is used to validate the numerical results.

- Flows over the circular spillways are simulated using three different turbulence models. The Standard k- ε model, RNG model, and RSM are used to obtain the velocity and pressure distributions of the flows over the spillways. To validate the results, two sets of experimental data done previously are used.

Chapter 2

Numerical Methods and Turbulent Flows

2.1 Introduction

Almost all fluid flows countered in engineering practice are turbulent. Turbulent flows are naturally unsteady, rotational, and three dimensional. In some fields such as hydraulics and environmental hydraulics, one deals with Newtonian, incompressible flows in which the 3D, time-dependent, incompressible continuity and Navier-Stokes equations govern:

$$\frac{\partial \widetilde{u}_i}{\partial x_i} = 0 \tag{2-1}$$

$$\frac{\partial \widetilde{u}_i}{\partial t} + \widetilde{u}_j \frac{\partial \widetilde{u}_i}{\partial x_j} = -\frac{1}{\rho}\frac{\partial \widetilde{p}}{\partial x_i} + \frac{\partial}{\partial x_j}(2\nu\widetilde{S}_{ij}) \tag{2-2}$$

In the above equations, compact tensor notation is used in the Cartesian coordinates. Here, $\widetilde{u}_i$ are the components of the instantaneous velocity and $\widetilde{p}$ is the instantaneous pressure. Also, ρ, ν, t, and x_j denote the fluid density, kinematic viscosity, time, and global Cartesian coordinates (j=1, 2, 3), respectively. The strain-rate tensor, $\widetilde{S}_{ij}$, is defined as follows:

$$\widetilde{S}_{ij} = \frac{1}{2}(\frac{\partial \widetilde{u}_i}{\partial x_j} + \frac{\partial \widetilde{u}_j}{\partial x_i}) \tag{2-3}$$

The most accurate approach to solve (2-1) and (2-2), is the Direct Numerical Simulation (DNS) by which all spatial and time scales of motions in the turbulence are calculated. Solving all scale motions by computers needs numerous processing speed and memory requirement. This makes DNS impractical in industry nowadays.

The second most accurate method is the Large Eddy Simulation (LES) in which the large eddies that carry the most turbulent energy are solved and small eddies are modeled. The small eddies are filtered out by filtering the velocity field and the accuracy of a LES depends on the size and type of filter. The time and storage demands for LES are less than those for DNS. However, large eddy simulations are time dependent and still need high-speed computers that make them expensive even though less costly than DNS to solve the same problem. Whenever it is feasible, DNS is the preferred method because it is more accurate than LES.

2.2 RANS Models

When a few quantitative properties of a turbulent flow are needed, the simpler models such as Reynolds-Averaged Navier-Stokes models can be used. When these models do not succeed or one needs a validity of results, DNS and LES should be used.

In the RANS approaches, all the unsteadiness is regarded as a part of the turbulence and is averaged out. With averaging (2-1) and (2-2), the conservation mass and momentum can be written as follows:

$$\frac{\partial u_i}{\partial x_i} = 0 \qquad\qquad (2\text{-}4)$$

$$\frac{\partial u_i}{\partial t} + u_j \frac{\partial u_i}{\partial x_j} = -\frac{1}{\rho}\frac{\partial p}{\partial x_i} + \frac{\partial}{\partial x_j}(2\nu S_{ij} + \tau_{ji}) \tag{2-5}$$

Here, u_i are the components of the averaged velocity and p is the averaged pressure. Also, the Reynolds-stress tensor, τ_{ij}, and the strain-rate tensor, S_{ij}, are defined as follows:

$$S_{ij} = \frac{1}{2}(\frac{\partial u_i}{\partial x_j} + \frac{\partial u_j}{\partial x_i}) \tag{2-6}$$

$$\tau_{ij} = -\overline{u_i' u_j'} \tag{2-7}$$

Here, $u_i' = \tilde{u}_i - u_i$ (fluctuating part of velocity). To close the equations (2-4) and (2-5), one needs to model the Reynolds-stress tensor (2-7). Non-isotropic turbulence models such as the Reynolds Stress Model (RSM) compute all components of (2-7) by which flows over the curved surfaces, secondary motions, flows with boundary-layer separation, and flows with highly curvilinear streamlines can be predicted properly with compared to isotropic turbulence models. On the other hand, when anisotropy of the Reynolds-stresses is negligible, isotropic turbulence models (such as two-equation models) based on Bousssinesq eddy-viscosity approximation can be used.

2.2.1 Reynolds Stress Model (RSM)

As a non-isotropic turbulence model, a RSM that is modified by Launder-Reece-Rodi is used in the present study (Launder, 1992):

$$\frac{\partial \tau_{ij}}{\partial t} + u_k \frac{\partial \tau_{ij}}{\partial x_k} = -G_{ij} + \frac{2}{3}\varepsilon \delta_{ij} - \Pi_{ij} - C_3 \frac{\partial}{\partial x_k}\left(\frac{k}{\varepsilon}(\tau_{i\ell}\frac{\partial \tau_{jk}}{\partial x_\ell} + \tau_{j\ell}\frac{\partial \tau_{ik}}{\partial x_\ell} + \tau_{k\ell}\frac{\partial \tau_{ij}}{\partial x_\ell})\right) \tag{2-8}$$

On the right-hand side of (2-8), the first term is the turbulent stress generation rate by the mean shear and is defined by (2-9). ε in the second term is the turbulence dissipation rate that is modeled by (2-10). The third term is the pressure-strain correlation that denotes the average product of the fluctuating pressure and strain fields and is modeled by (2-11). Turbulent diffusion transport is taken into account by the last term.

$$G_{ij} = \tau_{ik}\frac{\partial u_j}{\partial x_k} + \tau_{jk}\frac{\partial u_i}{\partial x_k} \tag{2-9}$$

$$\frac{\partial \varepsilon}{\partial t} + u_j\frac{\partial \varepsilon}{\partial x_j} = C_5\frac{\varepsilon}{k}\tau_{ij}\frac{\partial u_i}{\partial x_j} - C_6\frac{\varepsilon^2}{k} - C_4\frac{\partial}{\partial x_k}\left(\frac{k}{\varepsilon}\tau_{k\ell}\frac{\partial \varepsilon}{\partial x_\ell}\right) \tag{2-10}$$

$$\Pi_{ij} = C_1\frac{\varepsilon}{k}(\tau_{ij} + \frac{2}{3}k\delta_{ij}) - \frac{8+C_2}{11}(G_{ij} - \frac{2}{3}G\delta_{ij}) - \frac{8C_2-2}{11}(D_{ij} - \frac{2}{3}G\delta_{ij}) - \frac{60C_2-4}{55}k(S_{ij} - \frac{2}{3}\delta_{ij}S) + \Pi^w_{ij}$$

$$\tag{2-11}$$

$$\Pi^w_{ij} = \frac{k^{3/2}}{\varepsilon y}\left(0.125\frac{\varepsilon}{k}(\tau_{ij} + \frac{2}{3}k\delta_{ij}) - 0.015(G_{ij} - D_{ij})\right) \tag{2-12}$$

$$D_{ij} = \tau_{ik}\frac{\partial u_k}{\partial x_j} + \tau_{jk}\frac{\partial u_k}{\partial x_i} \tag{2-13}$$

Here, the turbulence kinetic energy $k = \tau_{ii}/2$, δ_{ij} is the Kronecker symbol ($\delta_{ij} = 1$ if $i = j$ and $\delta_{ij} = 0$ otherwise), $G = G_{ii}/2$, $S = S_{ii}/2$, and $y =$ distance normal to the solid surface. Also, $C_1 = 1.8$, $C_2 = 0.60$, $C_3 = 0.11$, $C_4 = 0.18$, $C_5 = 1.44$, and $C_6 = 1.92$.

2.2.2 k-ε Models

When anisotropy of the Reynolds-stresses is negligible, isotropic turbulence models based on Bousssinesq eddy-viscosity approximation that assumes the components of the

Reynolds stress tensor vary linearly with the mean rate of strain tensor can be used, as follows:

$$\tau_{ij} = 2\nu_T S_{ij} - \frac{2}{3}k\delta_{ij}$$ (2-14)

Here, ν_T is kinematic eddy viscosity. The most accurate isotropic turbulence models are two-equation models in which two transport equations are solved to determine the kinematic eddy viscosity, ν_T. The most popular two-equation models are k-ε models that model the kinematic eddy viscosity as follows:

$$\nu_T = C_\mu k^2 / \varepsilon$$ (2-15)

Turbulent kinetic energy, k, and dissipation rate of turbulent kinetic energy, ε, are determined by the following transport equations:

$$\frac{\partial k}{\partial t} + u_j \frac{\partial k}{\partial x_j} = \tau_{ij} \frac{\partial u_i}{\partial x_j} - \varepsilon + \frac{\partial}{\partial x_j}\left[(\nu + \nu_T / \sigma_k)\frac{\partial k}{\partial x_j}\right]$$ (2-16)

$$\frac{\partial \varepsilon}{\partial t} + u_j \frac{\partial \varepsilon}{\partial x_j} = C_{\varepsilon 1}\frac{\varepsilon}{k}\tau_{ij}\frac{\partial u_i}{\partial x_j} - C_{\varepsilon 2}\frac{\varepsilon^2}{k} + \frac{\partial}{\partial x_j}\left[(\nu + \nu_T / \sigma_\varepsilon)\frac{\partial \varepsilon}{\partial x_j}\right]$$ (2-17)

Here, $C_{\varepsilon 1} = 1.44$, $C_{\varepsilon 2} = 1.92$, $C_\mu = 0.09$, $\sigma_k = 1.0$, $\sigma_\varepsilon = 1.3$ in the Standard k-ε model (Ferziger and Peric, 2002).

The RNG k-ε model predicts the characteristics of near wall flows and flows in curved geometry boundaries with more accuracy than those of the Standard k-ε model. To solve the Reynolds-stress tensor of (2-14), the RNG k-ε model uses the same transport equations (2-16 and 2-17) with different coefficients that are appropriate to flows characterized by severe distortion encountered in highly curvilinear flows; $C_{\varepsilon 1} = 1.42$, $C_{\varepsilon 2}$

$$= C^*_{\varepsilon 2} + [C_\mu \lambda^3 (1-\lambda/\lambda_0)]/(1+\beta\lambda^3), \quad C^*_{\varepsilon 2} = 1.68, \quad \lambda = (k/\varepsilon)(2S_{ij}S_{ji})^{1/2}, \quad \beta = 0.012, \quad \lambda_0 = 4.38, \quad C_\mu =$$

0.085, $\sigma_k = 0.72$, and $\sigma_\varepsilon = 0.72$ (Yakhot and Smith, 1992).

2.3 Boundary Conditions

2.3.1 Free Surface Boundary

Free surfaces in open channel flows are the boundaries of two phases (air and water) that are moving in time. The shape of the water surface is not usually known in advance. For the initial condition, the free surface location is known but the boundary at later times should be determined as part of the solution.

Among many procedures, two major methods have been used to find the shapes of the free surfaces in open channel flows. In the first method, the free surface elevation is determined by allowing the computational mesh to deform during the iteration solution (Meselhe et al. 2000). This method treats the free surface as a sharp interface and the boundary-fitted grids are used. Therefore, the grids have to be justified in every time step when the boundary location is changed. The second method is the volume of fluid (VOF) that does not treat the free surface as a sharp boundary and does the computations on a fixed grid.

In the present study, the volume of fluid (VOF) scheme, which is an efficient method for treating the complicated free-surface problem (Mohapatra et al., 2001; Maronnier et al., 2003) was used to find the shape of the free surface. The shape of the free surface is determined by computing the fraction of each near-interface cell of a fixed grid that is partially filled (Ferziger and Peric, 2002). In addition to the governing equations of the

flow, a transport relation (2-18) for the filled fraction of every cell is solved to find the shape of the free surface.

$$\frac{\partial c}{\partial t} + \frac{\partial(cu_j)}{\partial x_j} = 0 \qquad (2\text{-}18)$$

Here, c is the filled fraction that changes from one for a cell full of water to zero for an empty cell. The pressure of the cells near the free surface boundary is obtained using linear extrapolation from the interior cells of the water domain.

Both fluids, water and air, can be treated as a single fluid. The properties such as density, molecular viscosity, and turbulence quantities of this single fluid (ϕ) are variables in every cell and can be calculated according to the volume fraction of each fluid as follows:

$$\phi = c\phi_w + (1-c)\phi_a \qquad (2.19)$$

ϕ_w and ϕ_a are the general properties of water and air, respectively.

2.3.2 Solid Boundary

At the wall boundaries, the wall function approach which relies on the existence of a logarithmic region in the profile of the axial velocity component was used (Launder and Spalding, 1974). The universal logarithmic law of the wall, applicable for $u_\tau y/v > 30$, is:

$$\frac{u}{u_\tau} = \frac{1}{\kappa}\ln\frac{u_\tau y}{v} + C \qquad (2.20)$$

Here, u_τ $(= \sqrt{\tau_w / \rho}\ )$ is the friction velocity, τ_w is the surface shear stress, $\kappa = 0.42$ is the von Karman constant, y is the normal distance to the solid surface, v is the kinematic viscosity, and $C = 5.45$ for smooth surfaces.

The kinetic energy generation and the turbulent energy dissipation rate are approximately in equilibrium at the wall-adjacent cells (Wilcox 2007). Therefore, when $k\text{-}\varepsilon$ models are applied, k and ε are obtained as follows:

$$k = \frac{u_\tau^{\ 2}}{\sqrt{C_\mu}}, \ \varepsilon = \frac{u_\tau^{\ 3}}{\kappa y} \qquad (2.21)$$

Here, y denotes the local coordinate that is normal to the solid surface. These boundary conditions are applicable for $u_\tau y / v > 30$.

When the Launder-Reece-Rodi model is used, the Reynolds stresses τ_{ij} and the turbulent dissipation rate ε at the wall-adjacent cells are computed from the following three dimensional boundary conditions applicable for $u_\tau y / v \approx 50$ (Launder and Li, 1994):

$$\tau_{xx} = -5.1 u_\tau^{\ 2}, \ \tau_{yy} = -1.0 u_\tau^{\ 2}, \ \tau_{zz} = -2.3 u_\tau^{\ 2}, \ \ \tau_{xy} = 1.0 u_\tau^{\ 2}, \ \ \varepsilon = \frac{u_\tau^{\ 3}}{\kappa y} \qquad (2.22)$$

Here, a local coordinate system was used. x and y denote the coordinates that are tangential and normal to the solid surface, respectively. z denotes the coordinate that is binormal to x and y.

2.3.3 Inlet and Outlet Boundaries

The velocity distribution is specified at the inlet boundaries. The turbulence quantities k and ε at the inlet boundary are estimated by the following equations:

$$k = \frac{3}{2} u_{avg}^2 I^2 \quad \text{and} \quad \varepsilon = C_\mu^{3/4} \frac{k^{3/2}}{0.07 D_h} \tag{2.23}$$

Here, u_{avg} is the average inlet velocity, I is the turbulence intensity that is typically between 1% to 5% and it depends on the upstream flow. Also, here, D_h (= $4R_h$) is the hydraulic diameter and R_h is the hydraulic radius of the conduit inlet cross section.

If the location of the outlet boundary is selected far away from geometrical disturbances, the flow reaches a fully developed state where no change occurs in the flow direction. In these situations that are normally possible, the gradients of all velocity components and turbulence quantities are zero. Also, these variables can be obtained using the linear extrapolation of computed values in the adjacent interior points that are just above the exit plane. If total mass flux are prescribed, the extrapolated velocity is then corrected to give the exactly the same total mass flux.

At the inlet boundary for open channels, the water surface level can be specified. At the outlet boundary, the water surface level can be specified or obtained using the linear extrapolation method.

To make the solution unique, one usually takes the pressure at a fixed point defined (reference pressure). Following this, the pressure correction calculated at that point is subtracted from all the corrected pressures.

2.4 Discretization Method and Solution Procedure

2.4.1 Finite Volume Method

The most common method to solve the governing and transport equations in computational fluid dynamics is the finite volume method (FVM). The computational domain is subdivided into a finite number of control volumes. The basic idea of FVM is to satisfy the integral forms of the governing and transport equations for every control volume in the domain as well as the whole domain. One of the most common schemes is the cell-centered scheme in which control volumes are identical with grid cells and the variables are associated with their centroids. The integration of the conservative form of all fluid flow equations can be written as follows:

$$\int_{cv} \frac{\partial(\rho\phi)}{\partial t} dV + \int_{cv} \vec{\nabla}.(\rho\phi\vec{U}) dV = \int_{cv} \vec{\nabla}.(\Gamma\vec{\nabla}\phi) dV + \int_{cv} S_\phi dV \qquad (2\text{-}24)$$

Here, ϕ is a general variable in the domain. $\phi = 1$ for the continuity equation. For the three components of momentum equations $\phi = u_i$ ($i = 1$, 2, and 3). Also, $\phi = k$, ε, and τ_{ij} in transport equations of turbulence models in 2.1.1 and 2.1.2. $\vec{U}$ is the velocity vector and S_ϕ is the source term. Γ is diffusion coefficient that equals dynamics viscosity μ for laminar flows, when $\phi = u_i$ and (2-24) becomes momentum equations. By applying divergence theorem, one can have (2-24) in the following form:

$$\frac{\partial}{\partial t}\left(\int_{cv}\rho\phi dV\right) + \int_{cs}(\rho\phi\vec{U}).\hat{n} dA = \int_{cs}\Gamma\vec{\nabla}\phi.\vec{n} dA + \int_{cv}S_\phi dV \qquad (2\text{-}25)$$

The first term on the left hand side of (2-25) signifies the rate of change of the total amount of fluid property ϕ in the control volume. The second term on the left is the rate of change of ϕ due to convection across the control volume. The rate of change of ϕ due to diffusion is represented in the first term on the right hand side. Finally, the last term gives the rate of change of the property ϕ as a result of sources.

To apply (2-25) and obtain an algebraic equation for each control volume, one needs to approximate the surface and volume integrals over the control volume surfaces and domain. To approximate the volume and surface integral by any numerical integration technique, the values of variables at locations other than computational nodes (cell centers) need to be approximated by interpolation. If the value of a variable at the cell center is used to calculate the volume integration, no interpolation is necessary. This is the second-order approximation that gives the exact results when the property in the control volume is either constant or varying linearly. An approximation of higher order to calculate the volume integrals requires the values of the variable at more locations than that at the center of the cell.

In this study, the collocated grid arrangement that is suitable for non-orthogonal body-fitted mesh is used. In collocated grid arrangement (Rhie and Chow, 1983), the same control volumes are used for all equations and all variables are stored at the same grid points. Therefore, interpolation methods are needed to find the values of the variables at some locations of the control volumes surfaces. To calculate the surface integrals, one needs to interpolate the values of variables at least at the centers of the control volume surfaces.

First-order upwind interpolation (upwind difference scheme, UDS) is a simple and useful scheme to interpolate the surface center value of a variable. It unconditionally satisfies the boundedness criterion that never yields oscillatory solutions. If a suitable mesh is selected, the first-order upwind scheme can be used for the convective term in (2-25) and the results are accurate for flows with high Reynolds numbers. The linear interpolation scheme that approximates the value of the variable at the surface center of a cell by interpolation between two nearest nodes (central difference scheme, CDS) is second-order accurate. Although this scheme may produce oscillatory solutions, it is the simplest second-order method that is more accurate and is the one most widely used especially for the diffusion term in (2-25). In this study, UDS and CDS are used for the convective and diffusion terms, respectively.

Other schemes such as quadratic upwind interpolation and higher-order interpolation may be used to calculate the values of a variable at the cell-face centers. For higher-order approximation of the surface integrals, the variables must be evaluated at corners of the cells too. This can be done after determining the values at the cell-face centers. More details of FVM are given in the relevant references (Ferziger and Peric, 2002; Versteeg and Malalasekera, 2007).

2.4.2 Solution Procedure and Pressure-Correction Methods

To calculate all variables including pressure, velocity components, and turbulent quantities, one needs to solve the system of non-linear equations (continuity, momentum, and turbulent transport equations). Direct solution of non-linear coupled equations is very complicated. Because of that, these equations have to be linearized and then solved by an iteration method. Another important problem is that if one wants to solve all coupled

equations simultaneously, it would make convergence very difficult to reach. Therefore, an outer iteration of RANS equations (2-4 and 2-5) in which the values of the turbulent properties are based on their values at the end of the preceding iteration is performed. And then, another outer iteration of the turbulent transport equations is made. To avoid numerical instability and guarantee the convergence, under-relaxation parameters are needed for all equations when each equation is solved separately by an iteration method (inner iteration). In an outer iteration, RANS equations (2-4 and 2-5) have to be solved to calculate the pressure and the velocity components.

Solving these equations is complicated because there is not an independent equation for the pressure. In compressible flows the continuity equation can be used to determine the density and the pressure is calculated from an equation of state. This method can not be used for incompressible flows. For incompressible flows, one can solve the momentum equations one by one or simultaneously by using the values of pressure from the proceeding inner iteration. Then, the velocity components and pressure can be corrected by satisfying the continuity equation (pressure-correction equation). This approach is called the pressure-velocity coupling method.

The first and most popular solution algorithm for pressure and velocity calculation is called SIMPLE (Semi-Implicit Method for Pressure-Linked Equations) that was put forward by Patankar and Spalding (1972).

For every outer iteration, the first step is to solve the linearized momentum equations in which the pressure field, the velocity values included in the coefficients as well as the turbulent quantities are assumed from the previous iteration. The new calculated velocity values do not satisfy the continuity equation. The pressure correction is defined as the

difference between correct pressure that is unknown and the guessed pressure that assumed from the previous iteration. Also, the velocity corrections are defined as the difference between correct velocities that are unknown and the guessed velocities that calculated from the first step. The correct, unknown pressure and velocities are substituted in the momentum equations. Then, by subtracting the two sets of the momentum equations and applying the continuity equation, an equation can be derived in which the only unknown is the pressure correction and a term including the velocity corrections (a Poisson equation).

As the second step, one needs to solve the Poisson equation (the pressure-correction equation), compute the velocity corrections, and calculate the new values of velocities and pressure. In the derived Poisson equation, the term including the unknown velocity corrections is omitted. Due to neglecting this term, the SIMPLE algorithm does not converge rapidly and one needs to use under-relaxation for the Poisson equation. With the new values of pressure and velocities, the turbulent transport equations can be solved. Because the new values of the variables do not satisfy the momentum equations, the second iteration should be started from the first step and continued to reach the convergence.

Patankar (1980) introduced an improved version of SIMPLE that is called SIMPLER (SIMPLE Revised) algorithm in which the continuity equation is used to derive an equation for the pressure, instead of a pressure correction equation as in SIMPLE. Although the number of calculations involved in SIMPLER is larger than that in SIMPLE, the fast convergence rate reduces the computer time (Versteeg and Malalasekera, 2007).

The SIMPLEC (SIMPLE-Consistent) algorithm follows the same steps as the SIMPLE algorithm, with the difference that the velocity corrections term in the pressure correction equation is approximated rather than being neglected (van Doormal and Raithby, 1984).

Issa (1986) presented PISO (Pressure Implicit with Splitting of Operations) algorithm in which there are two corrector steps. The first step of PISO is the same as in SIMPLE. In the second step, at first, the pressure correction equation is solved (the velocity correction term is neglected here too), the velocity corrections are calculated, and the velocity and pressure values are computed as by SIMPLE. At this stage, a second pressure correction equation including the velocity corrections term is solved (the velocity corrections are approximated by solving the first pressure correction equation). Finally, the twice-corrected velocity field along with the pressure field is obtained. The next outer iteration is started from the first step and will be continued to reach the convergence (Ferziger and Peric, 2002). PISO can maintain a stable calculation with a larger time step in transient flows. In the present study, PISO algorithm is adopted.

2.4.3 Grid Generation; Solution Accuracy

Grid Generation

Solving the fluid flow equations are based on discretization procedures such as FVM in which one needs to divide the domain to a numerous cells and create a mesh system. For a regular geometry, an orthogonal (Cartesian, cylindrical, spherical, etc.) mesh whose lines follow the coordinate directions may be used. The extension of the discretization methods to orthogonal coordinates is relatively straightforward. However, many engineering problems in fluid mechanics involve complex geometries.

A complex geometry can not be fitted in one of the above coordinates. To avoid inaccuracy of the results because of approximating the geometry, non-orthogonal body-fitted (structured or block-structured) grids are needed for the problems involving complex geometries (Versteeg and Malalasekera, 2007). The more flexible mesh that can be used for the domains with very complex geometries is unstructured grid arrangement in which every individual cell can be considered as a block and is not restricted to one particular cell type. In most cases, using a suitable unstructured mesh can give more accurate results than that of structured one. However, the solvers for the algebraic equation systems are usually slower than those for other grids.

In this study, non-orthogonal, block-structured mesh systems along with the collocated arrangement are used. Also, each block is meshed using power law functions. Power law function allows user to make the mesh finer near the boundaries or in the regions where the gradients of the variables are high. It should be noted that the first grid point needs to be within the logarithmic region defined by wall functions in section 2.2.2.

Solution Accuracy

To enhance the accuracy of the results, a suitable discretization method such as finite volume method (that approximates the transport equations) is needed. The first key of achieving an accurate result is to approximate the integrations and perform the interpolations properly (Section 2.3.1). In this study, steady flows are modeled as transient flows and solved using iteration methods. The second key for obtaining an accurate result is to decrease the iteration errors (convergence errors). The difference between the exact solution and iterative solution of the discretized equations is defined as the iteration error. In practice, the available computing power and time dictate that one

truncates the iteration sequence when the solution is sufficiently close to the final solution. In this study, the relative global residual of each variable (difference between successive iterates) is monitored to control the convergence. The relative residuals are kept at 0.0001 to 0.00001 for all variables. Also, the inflow and outflow fluxes are controlled. Besides, the temporal rate of change of velocity values at some points are examined to be negligible for convergence. To achieve a fast convergence, one should divide the domain with a suitable mesh according to the gradients of the variables in different regions.

Also, the grid sensitivity or grid independence needs to be checked. The results of each simulation were checked for grid independence using a coarser grid whose cells dimensions were twice as those of the final grid cells sizes. Also, the results were checked using a finer grid whose cells dimensions were half as those of the final grid cells sizes. The results of the coarser grid size were in less agreement than the results related to the final grid. Further, the results for the finer grid were essentially the same as the case of the final grid chosen. The deviations of velocities and pressures were generally much less than 1% between the results obtained from the final grid and the finer grid.

Chapter 3

Turbulence Modeling of Flows through Cut-throat Flumes

3.1 Introduction

The determination of the discharge rate in open channels is an essential aspect of water resources management. Among critical flumes which are used to measure discharge rates in irrigation systems and water treatment plants (Ackers et al. 1978; Bos 1989), cut-throat flumes are simple devices that are easy to construct. These flumes have horizontal floors with the same upstream and downstream widths and without a throat length (Fig. 3.1). The flow in the throat region of the cut-throat flume is highly curvilinear, as the flow accelerates from the subcritical regime to the supercritical regime. Further, in this region, flow is highly three dimensional.

The characteristics of flow in cut-throat flumes have been studied in the past by several investigators. The cut-throat flume was developed by Skogerboe and Hyatt (1967). Keller (1981) studied the non-similarity entrance features on the characteristics of the flow in cut-throat flumes. Keller (1984) also conducted systematic tests on cut-throat flumes and published results that have direct field applications. Ramamurthy et al. (1985) developed an equation to calculate the discharge rate of free flows in these flumes based on the depth of the approaching flow. Ramamurthy et al. (1988) developed a semi-empirical relationship between the non-dimensional discharge and the upstream flow depth for submerged cut-throat flumes by using the momentum equation.

In this chapter, the turbulence Reynolds Stress Model (RSM) is applied to analyze the characteristics of flow through cut-throat flumes in rectangular open channels. RSM provides physically realistic predictions especially for three dimensional flows with highly curved streamlines (Wilcox, 2007). The three-dimensional finite volume discretization was used for the numerical simulation.

The existing experimental data of Aukle (1983) and Keller and Mabbett (1987) were used to validate most of the results. To verify the 3D nature of the flow predicted by the model, a few experimental results were also obtained based on a new test.

3.2 Experimental Data

Three sets of experimental data are used to validate the predictions of the turbulence model; the experimental data of Aukle (1983), the test data of Keller and Mabbett (1987), and a new test.

Aukle (1983) used three geometrically similar rectangular cut-throat flumes were set in a channel with horizontal floors. The flumes had the same upstream and downstream widths and without a throat length (Fig. 3.1 and Table 3.1). The pressure heads at some points along the flumes centerlines were measured by static pressure probe. A standard pitot tube was used to obtain the streamwise velocity distributions at some vertical sections along the flumes centerlines. Also, surface profiles were measured by means of point gages at centerlines. Also, the discharges are obtained using a standard 60° V-notch weir.

Keller and Mabbett (1987) constructed a horizontal flume and a total of 46 test runs were carried out. For every test run, the flow rate was measured using electro-magnetic

flowmeter. Very low flow rates are obtained by weighting the water discharged during the determined time interval. The corresponding upstream head pressures in the flume were collected by a submersible differential pressure transducer located in stilling well.

A new cut-throat flume with $L = 0.474$, $B = 0.285$, and $B_T = 0.178$ m (Fig. 3.1) was also setup in an existing glass flume that was modified specially to study briefly a few aspects of three dimensionality of the flow. In this new test, the upstream depth of flow was 0.094 m. At a section 0.05 m ($= 0.175$ B) downstream of the flume exit, the spanwise and vertical velocity components were measured using a Laser Doppler Velocimetry (LDV).

3.3 Solution Procedure

The collocated finite volume method was used to approximate the governing equations to algebraic equations that can be solved numerically. The pressure-velocity coupling scheme was achieved using the PISO (Pressure-Implicit with Splitting of Operators) algorithm (Issa, 1986).

The computational domain for the numerical simulation is shown in Fig. 1 for three geometrically similar flumes. In the simulation, for each flume, four to five different depths of flows were chosen. These were the same flow parameters as in the experiments (Ramamurthy et al., 1985, and Aukle, 1983). The lengths of the channel upstream and downstream of the cut-throat flume were 2.438 m and 0.305m, respectively. Values of L, B, B_T, upstream depths of flows, and discharges for all the three flumes are given in Table 3.1. The entrance 3-3 of the cut-throat flume is at $x_l = 0.305$ (Fig. 3.1). Further, the flow depth in the flume I was set at 0.130 m for one test in which the streamwise velocity distributions at some vertical sections were measured. The flow domain was meshed with

a power law function that generates the finer mesh close to the channel boundaries. The first grid cell rows next to the walls were constructed well within the logarithmic region $30 < u_*y/\nu < 100$. The results were checked for grid independence using a coarser grid whose cells dimensions were twice as those of the final grid cells sizes. Also, the results were checked using a finer grid whose cells dimensions were half as those of the final grid cells sizes. The results of the coarser grid size were in less agreement than the results related to the final grid. Further, the results for the finer grid were essentially the same as the case of the final grid chosen. The deviations of velocities and pressures were generally much less than 1% between the results obtained from the final grid and the finer grid. Through the time-dependent simulation, water flows in the open channel and constitutes the free surface between air and water.

The VOF scheme is used for the free surface boundary (Sec. 2.2.1). The standard wall functions are used for the solid boundaries, bottom and walls (Sec. 2.2.2). The depth of flow, average velocity and the quantities of the turbulence are known at the inlet boundary (Fig. 3.1; Sec. 2.2.3). At the outlet (Fig. 3.1) that is enough far away from the exit of the throat, water surface obtained using the linear extrapolation method and the gradients of all velocity components and turbulence quantities set to zero.

3.4 Results

Existing experimental results (Ramamurthy et al., 1985 and Aukle, 1983) related to water surface profiles, pressure distributions, and streamwise velocity distributions for flow in cut-throat flume were used to validate the numerical simulation predictions. For water surface profiles along the flume centerlines, Fig. 3.2 shows that there is a good agreement

between numerical predictions and experimental results. The agreement is equally good in both the subcritical and supercritical flow regions. Both experimental and predicted pressure head distributions along the centerlines of the flumes are shown in Fig 3.3. The simulation results agree well with the experimental data. Fig. 3.4 displays the few available vertical distributions of the streamwise velocity along the centerline of the flume *I*. There is a small disagreement between the numerical predictions and the experimental results near the free surface at the throat section (Fig. 3.4). The disagreement between test data and model predictions can be traced in part to the use of the Pitot tube for velocity measurements close to the free surface.

Fig. 3.5 shows the resultant of the lateral and vertical mean velocities at a section 0.05 m (=0.175B) downstream of the flume exit. Because the maximum deviations of the lateral and vertical velocity components measured in the sections right and left of the channel centerline were relatively small (< 0.01 m/s), only data of one half of the cross section are used for model validation (Fig. 3.5). The numerical model predicts the cross water surface profile of the three dimensional flow well and the secondary flow reasonably well.

Keller and Mabbett (1987) have provided dimensionless parameters characterizing the flow behavior in cut-throat flumes. According to them, the non-dimensional discharge and non-dimensional head parameters are defined as follows:

$$Q_N = \frac{Q}{\sqrt{g}\, B_T\, h_0^{1.5}} \quad, \quad h_N = \frac{h_0}{B_T} \tag{3.1}$$

Here, Q and h_0 are discharge of approach flow and pressure head at section *2-2* (Fig. 3.1), respectively. The present numerical results compare well with the experimental results of

Keller and Mabbett (1987) presented in terms of dimensionless parameters Q_N and h_N (Fig 3.6).

3.5 Conclusions

The three dimensional RSM along with the VOF scheme can properly reproduce the mean characteristics of flow in cut-throat flumes. These characteristics include the water surface profile, pressure distributions, and streamwise velocity distributions. Also, the model faithfully predicts the secondary flow downstream of the throat. The predictions of the numerical model agree well with the existing experimental results. Due to lower time demand and lower cost of numerical methods compared to experimental methods in predicting the flow characteristics, simulation of the cut-throat flume flows based on a properly validated model provides the flow characteristics of these flumes for various flow configurations encountered in the field.
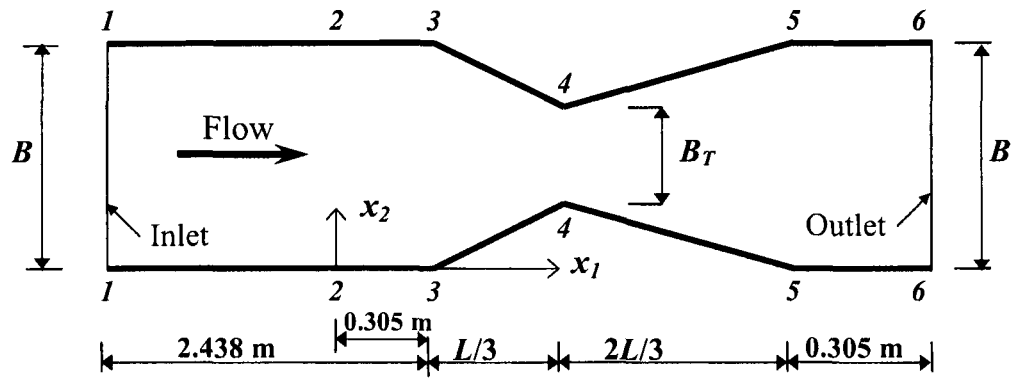
Fig. 3.1. Computational domain for

Cut-throat Flume, plan
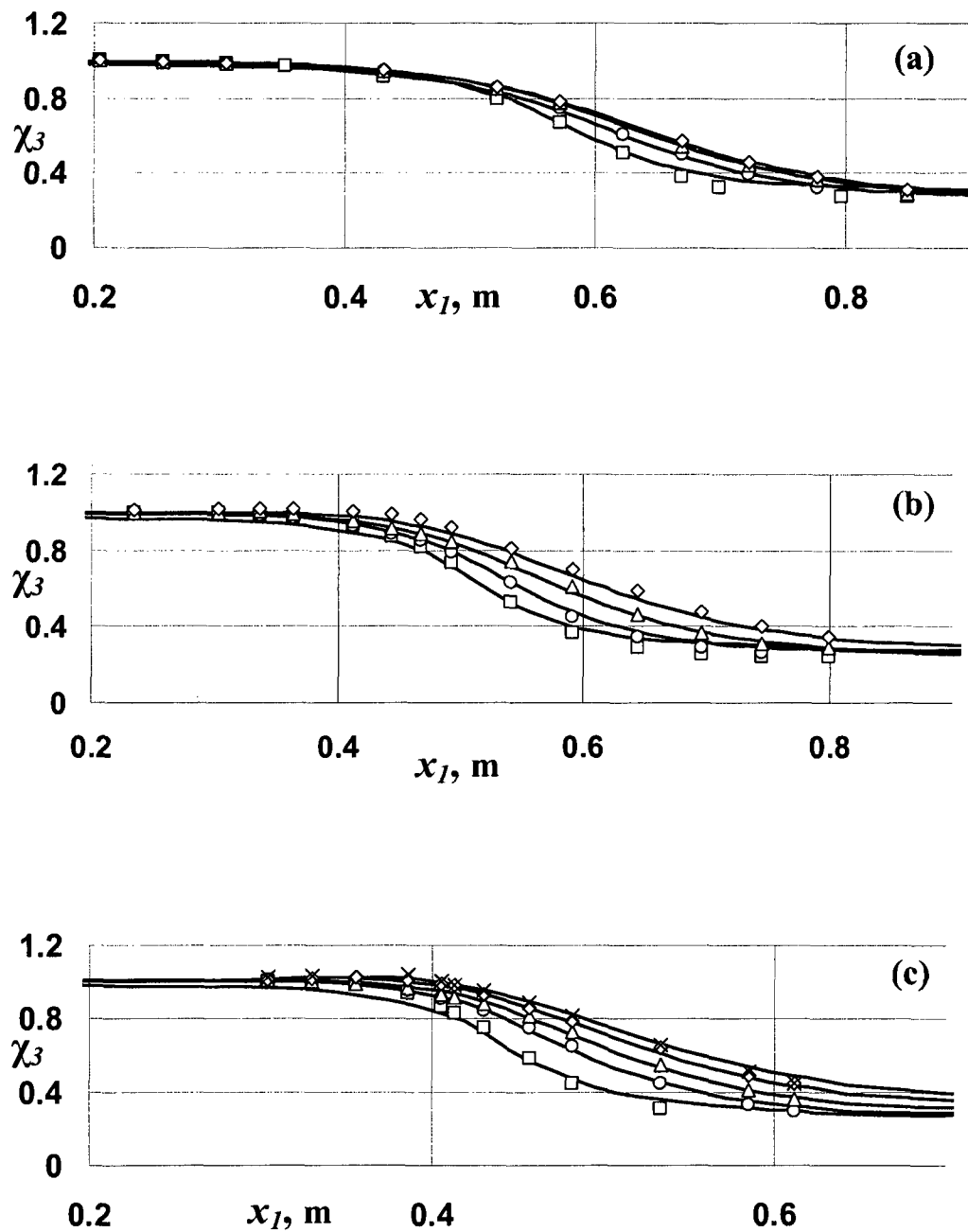
Fig. 3.2. Water surface profiles, a) Flume *I*, b) Flume *II*, c) Flume *III*

— Numerical Simulation

Exp. (Aukle, 1983): □ Test 1, ○ Test 2, △ Test 3, ◇ Test 4, X Test 5
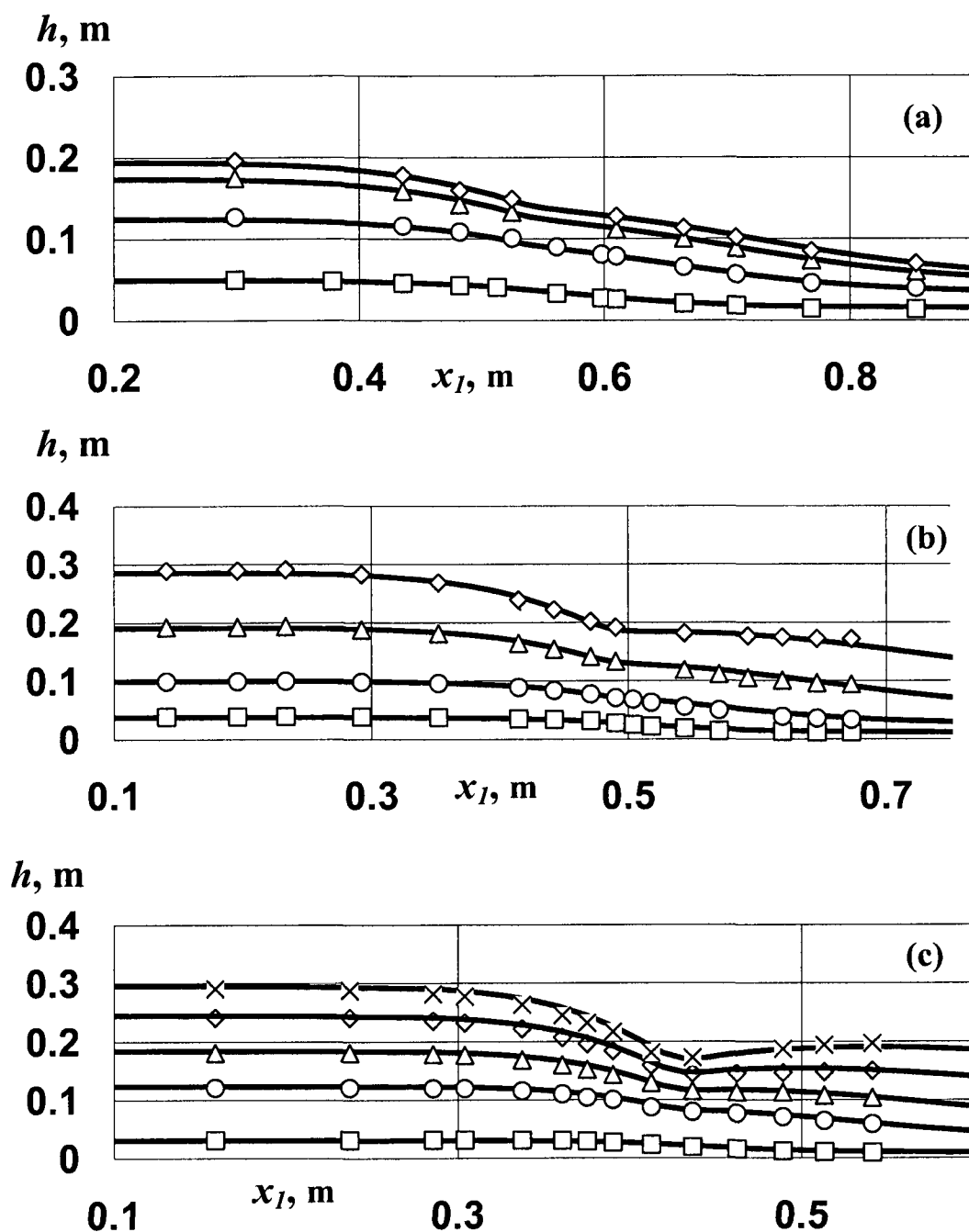
Fig. 3.3. Pressure distribution along the flume centerline, a) Flume I, b) Flume II, c) Flume III

— Numerical Simulation

Exp. (Aukle, 1983):   □ Test 1,   O Test 2,   △ Test 3,   ◇ Test 4,   X Test 5
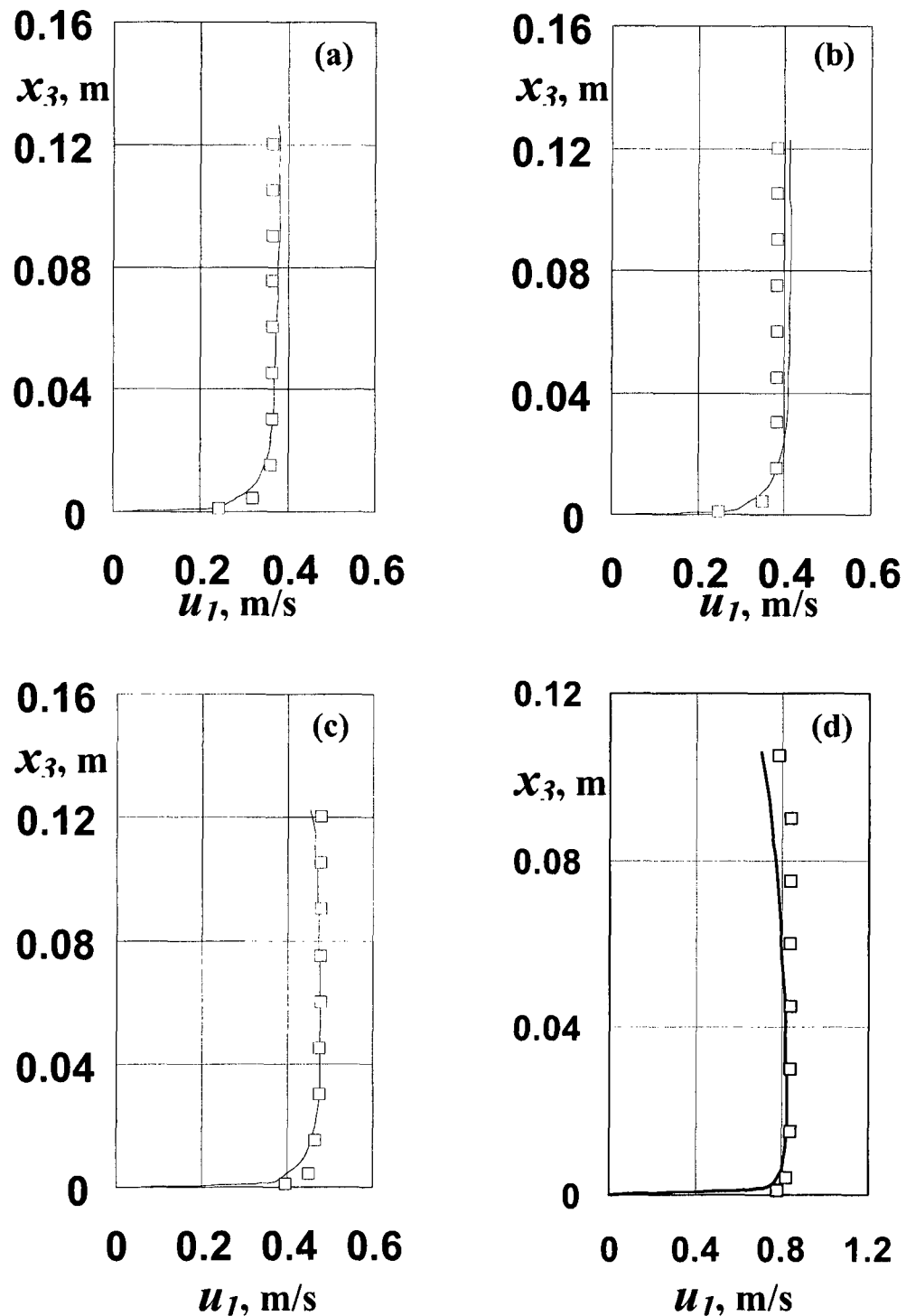
Fig. 3.4. Streamwise velocity distribution along the flume centerline

a) $x_1 = 0$, b) $x_1 = 0.305$ m (entrance of the flume),

c) $x_1 = 0.305$ m $+ L/9$, d) $x_1 = 0.305$ m $+ L/3$ (throat section)

— Numerical Simulation, □ Exp. Data (Aukle, 1983)
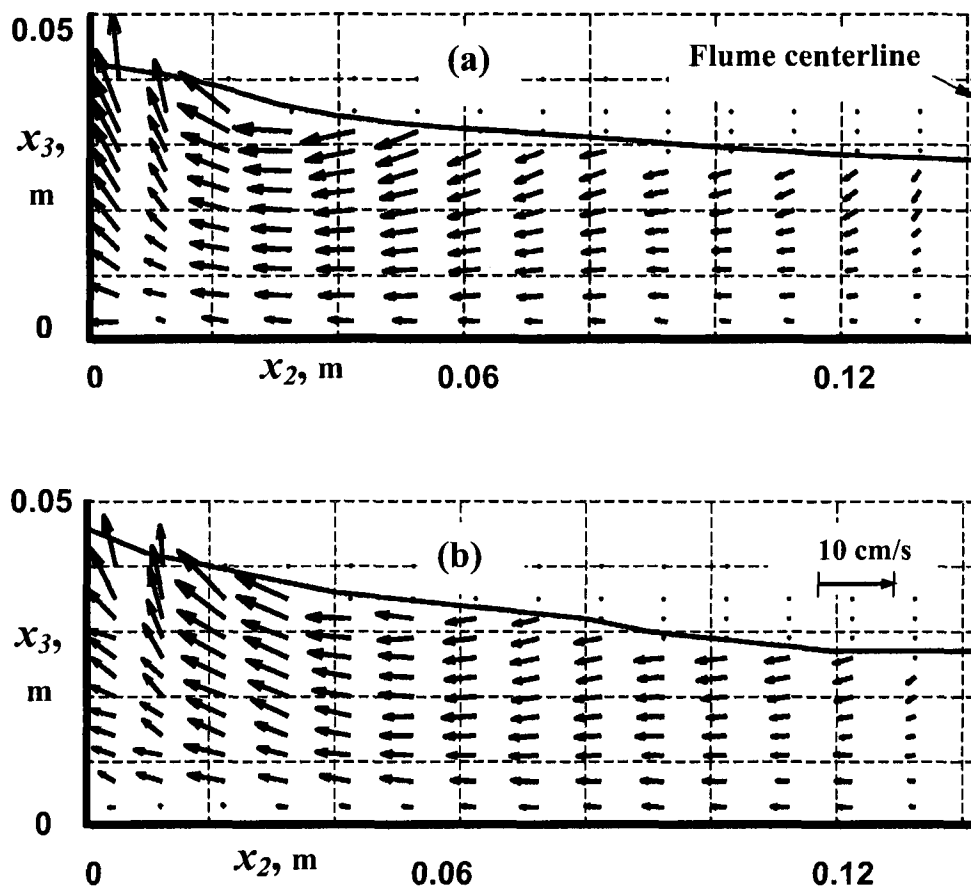
Fig. 3.5. Secondary flow at a cross section

0.175 B downstream of the flume exit

a) Numerical Simulation   b) Test Data
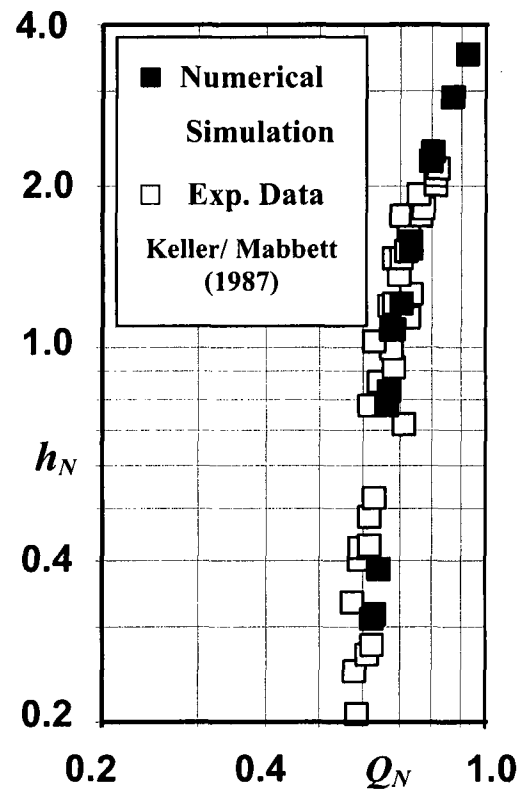
Fig. 3.6. Non-dimensional data

Flume	L, m	B, m	B_T, m	Test number	u/s Flow depth, m	Flow rate, L/s
I	0.648	0.300	0.156	1	0.050	3.23
				2	0.127	13.61
				3	0.175	23.06
				4	0.196	27.80
II	0.486	0.225	0.117	1	0.039	1.64
				2	0.100	7.63
				3	0.193	21.01
				4	0.289	41.34
III	0.324	0.150	0.078	1	0.032	0.82
				2	0.123	7.29
				3	0.183	14.16
				4	0.244	23.13
				5	0.298	32.25

Table 3.1. Values of 'L' and 'B' in Fig. 3.1 for different flumes

and depths of flow at $x_1 = 0$ for different tests (Aukle, 1983)

Chapter 4

Numerical Simulation of Flows over Lateral Weirs

4.1 Introduction

A lateral weir, also known as a side weir, is a simple structure often used in urban and land drainage works, irrigation systems, and flood protection practices. The flow in the region of the side weir is three dimensional and the streamlines are highly curved. Further, in this region, there is a stagnation line very close to the downstream edge of the weir and a small area of reverse flow is present there. The RANS models based on Boussinesq eddy viscosity hypothesis assumes linear variation of the components of the Reynolds stress tensor with the mean rate of strain tensor. These can not properly predict the characteristics of complex, three dimensional flows as in side weir flows (Bates et al, 2005). As such, the three dimensional turbulence Reynolds Stress Model (RSM) was used in the present study.

In the past, several investigators have studied the behavior of lateral weirs. De Marchi (1934) assumed that the total energy remains unchanged along the weir and obtained an empirical equation to find the side weir discharge in a rectangular channel as follow:

$$q_s = \frac{dQ_s}{dx_1} = \frac{2}{3} C_m \sqrt{2g} \left(x_3 - s \right)^{3/2} \tag{4-1}$$

Here, Q_s is the discharge of the weir, q_s is the weir discharge per unit length, x_1 is the streamwise distance from the upstream edge of the weir, g is the gravitational

acceleration, s is the height of the weir crest from the channel bed, x_3 is the depth of flow at the section x_1 (Fig. 4.1), and C_m is De Marchi coefficient. C_m can be expressed as follow:

$$C_m = f\left(F_{r1}, \frac{L}{B}, \frac{s}{d_0} \right) \tag{4-2}$$

Here, F_{r1} is the upstream Froude number, L and B are the length of the weir and the width of the rectangular channel, respectively, and d_0 is the depth of flow upstream the weir. Based on the De Marchi equation, Subramanya and Awasthy (1972), Nadesamoorthy and Thomson (1972), Raga Raju et al. (1979), Hager (1982 and 1987), and Uyumaz and Smith (1991), considered F_{r1} as the main parameter influencing C_m. Ramamurthy and Carballada (1980) considered F_{r1}, L/B, and s/d_0 in the analysis of side weir flows. Singh et al. (1994) found the Froude number and s/d_0 to be effective in determining C_m. They obtained a linear dependence of C_m on F_{r1} and s/d_0. Borghei et al. (1999) presented an empirical equation that satisfied (4.2) covering all three non-dimensional parameters. Muslu (2001) and Muslu et al. (2003) considered the effect of lateral water surface profile on the side weir discharge. Generally, one has to start with De Marchi equation and go through complicated steps to find C_m and finally obtain the side weir discharge. Ramamurthy et al. (2006) used the nonlinear partial least square method and existing experimental data to obtain a forth-order polynomial equation to get the De Marchi coefficient.

In the present study, the turbulence Reynolds Stress Model (RSM) was applied to analyze the characteristics of flow in a rectangular open channel in which a side weir is located. RSM provides physically realistic predictions especially for three-dimensional flows with

highly curved streamlines and stagnation lines (Wilcox, 2007). The three-dimensional finite volume discretization was used for the numerical simulation. The experimental data of Hager (1982) and Subramanya and Awasthy (1972) were used to validate the results.

4.2 Experimental Data

Two sets of experimental data are used to validate the predictions of the turbulence model; the experimental data of Hager (1982), the test data of Subramanya and Awasthy (1972).

The models of Hager (1982) were set up in a rectangular channel of width = 30 cm and total length = 5.70 m, which includes the lateral weirs of different heights (Fig. 4.1). The length of the side weirs L = 1.00 m. The corresponding parameters of four test runs considered for validation of the numerical results are given in the Table 4.1.

Subramanya and Awasthy (1972) used two horizontal rectangular flumes to investigate the flows in channels with side weirs. One of the flumes had a cement plaster bed and the second one an aluminum bed. The data of the later has used to validate the streamwise velocity predictions by numerical simulation. This flume was 3.00 m long and 24.8 cm wide. The length of the side weir was 15 cm with no sill. The depths of flow in the channels were measured by point gages.

4.3 Solution Procedure

The finite volume method (FVM) with a collocated grid arrangement was used to approximate the governing equations to algebraic equations that can be solved numerically. The pressure-velocity coupling scheme was achieved using the PISO (Pressure-Implicit with Splitting of Operators) algorithm (Issa, 1986).

The computational domain for the numerical simulation is shown in Fig. 4.1 (in accordance with the Hager's experiment, 1982). The length, L_{1-2}, and the width, B, of the channel were 5.70 m and 0.30 m, respectively. The length of the side weir, L, is 1.000 m. Other corresponding parameters are given in Table 4.1.

Fig. 4.4 shows the computational domain used for numerical simulation of experimental model done by Subramanya and Awasthy (1972). The length and width of the channel and the side weir length are 2.850, 0.248, and 0.150 m, respectively. The locations of the sections A-A, B-B, and C-C (Fig. 4.4) are $x_2 = 0.034$, 0.124, and 0.186 m, respectively.

The flow domain was meshed with a power law function that generates the finer mesh close to the channel boundaries. The first grid cell rows next to the walls were constructed well within the logarithmic region $30 < u_\tau y/v < 100$. The results were checked for grid independence using a coarser grid whose cells dimensions were twice as those of the final grid cells sizes. Also, the results were checked using a finer grid whose cells dimensions were half as those of the final grid cells sizes. The results of the coarser grid size were in less agreement than the results related to the final grid. Further, the results for the finer grid were essentially the same as the case of the final grid chosen. The deviations of parameters were generally much less than 1% between the results obtained from the final grid and the finer grid. Through the time-dependent simulation, water flow gets established in the open channel and forms the free surface between air and water.

The standard wall functions are used for the solid boundaries, bottom and walls (Sec. 2.2.2). The VOF scheme is used for the free surface boundary (Sec. 2.2.1). The average velocity and the quantities of the turbulence as well as water surface location are specified at the inlet boundary (Fig. 4.1; Sec. 2.2.3). At the downstream outlet (Fig. 4.1)

that is enough far away from the weir region, water surface are known according to the experiments. The gradients of all velocity components and turbulence quantities are zero at the downstream outlet. Also, at the weir outlet, all parameters are calculated by linear extrapolation method.

4.4 Results

Existing experimental results (Hager, 1982) related to water surface profiles and channel discharge rates were used to validate the numerical simulation predictions. For water surface profiles along the centerline of the channel, Fig. 4.2 shows that there is a good agreement between numerical predictions and experimental results. Both experimental and predicted channel discharge rates are shown in Fig 4.3. The simulation results agree well with the experimental data for all the four runs considered.

Fig. 4.4 displays the side weir configuration with no sill used by Subramanya and Awasthy (1972). The vertical distributions of the streamwise velocities at a few locations are used for model validation. The agreement between the numerical and the experimental results are quite good (Fig. 4.5).

4.5 Conclusions

A three dimensional RSM together with the VOF tracking method faithfully determines the characteristics of side weir flows including flow rates, water surface profile, and velocity distributions. The predictions of the model are validated using the experimental results. Lower time demand and lower cost are associated with numerical methods. As such, simulation of the side weir flows based on a properly validated numerical model provides a simple procedure to determine the flow characteristics of these flows, for

various flow configurations that one encounters in engineering practice, without recourse

to expensive experimental procedures.
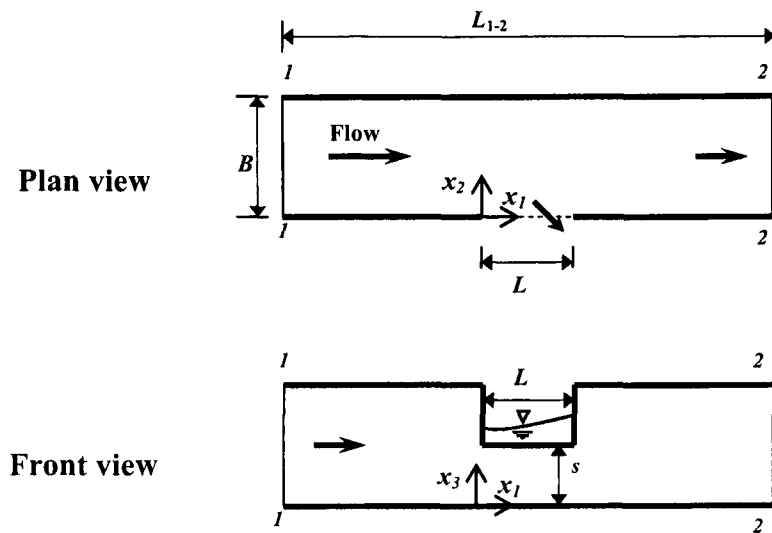
Fig. 4.1. Sketches of side weir
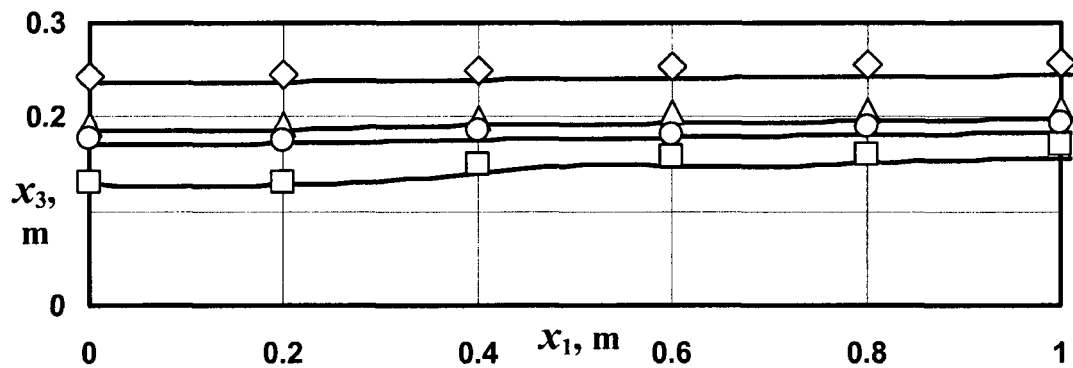
Fig. 4.2. Water surface profiles

Numerical Simulation   —

Exp. Data (Hager, 1982): □ Run D, Δ Run E, ◊ Run F, O Run G
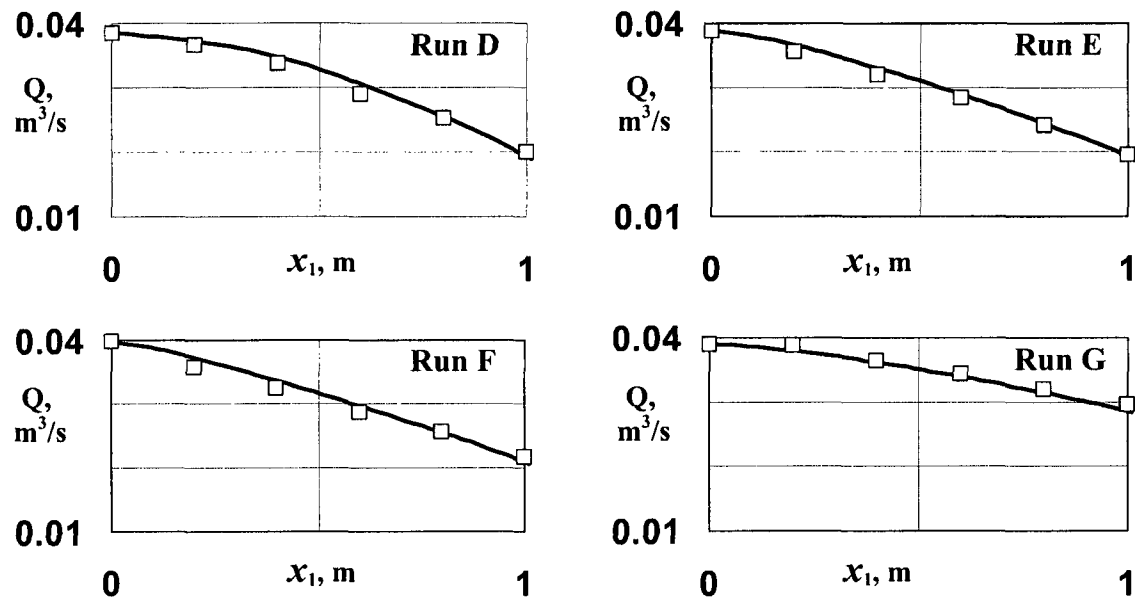
Fig. 4.3. Channel discharge rates

— **Numerical Simulation,** □ **Experimental Data (Hager, 1982)**
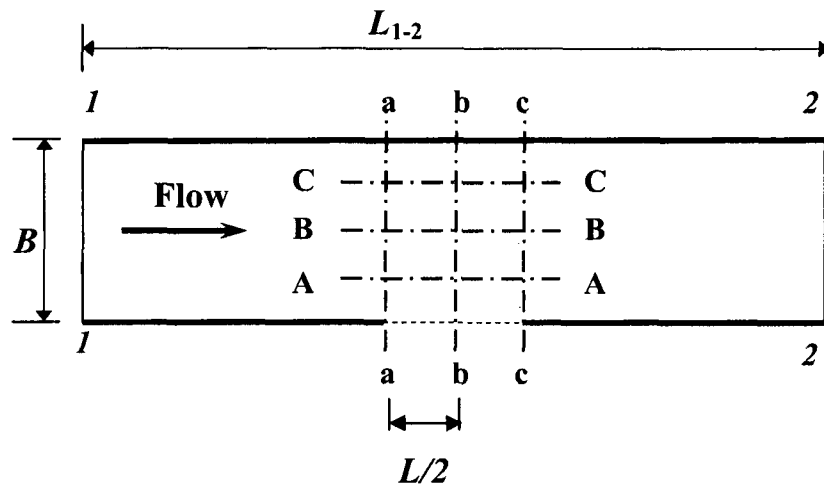
Fig. 4.4. Plan view of side weir without a sill; grid points for velocity measurement (Subramanya and Awasthy, 1972)
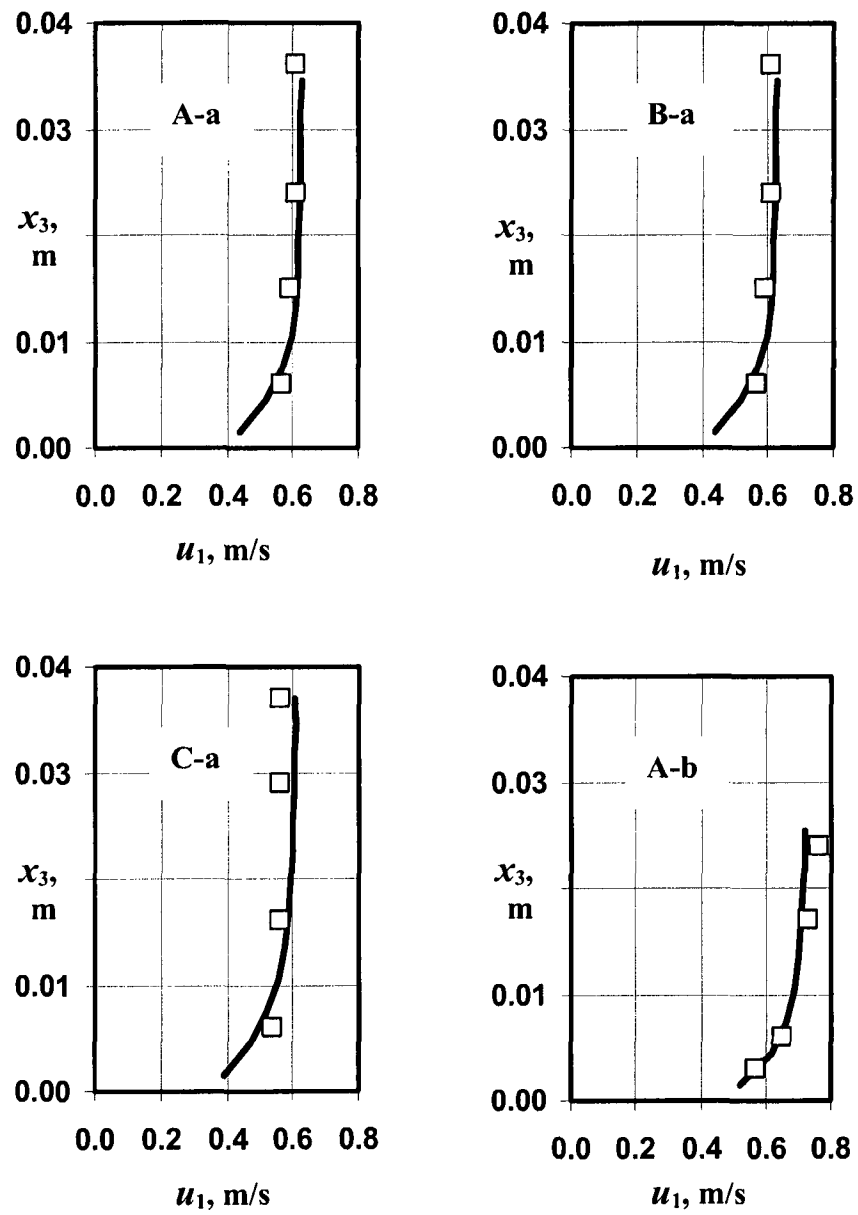
Fig. 4.5. Streamwise velocity profiles (Fig. 4.4)

— Numerical Simulation,

□ Experimental Data (Subramanya et al., 1972)
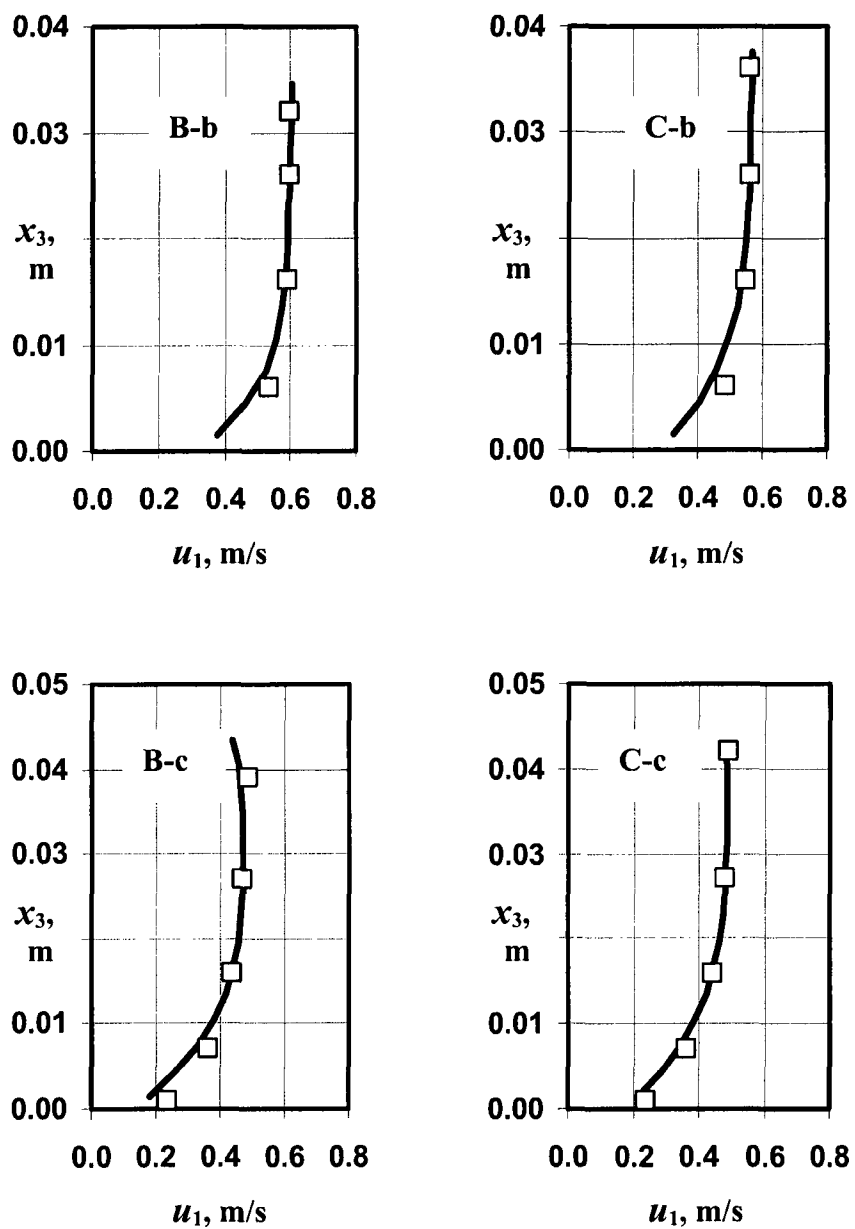
Fig. 4.5. (cont.) Streamwise velocity profiles (Fig. 4.4)

— Numerical Simulation,

☐ Experimental Data (Subramanya et al., 1972)

Test	Sill s (m)	u/s flow depth (m)	d/s flow depth (m)	u/s flow rate (m)	d/s flow rate (m)
D	0.10	0.130	0.171	38.55	20.03
E	0.15	0.192	0.209	38.87	19.52
F	0.20	0.244	0.257	39.79	21.70
G	0.15	0.177	0.194	39.06	29.60

Table 4.1. Experimental parameters (Fig. 4.1; Hager, 1982)

Chapter 5

Numerical Simulation of Sharp-Crested Weir Flows

5.1 Introduction

The sharp-crested weir in a rectangular open channel (Fig. 5.1) serves as a simple and accurate device for flow measurement in open channels. It also enables one to control and regulate open channel flows. Further, the lower nappe profile of the weir is often considered as the shape of spillway profile. A large number of theoretical and experimental studies have been carried out to know the weir characteristics. Rouse and Reid (1935) made an analytical investigation of the design of spillway crests based on the investigation of sharp-crested weir flow characteristics. Kandaswamy and Rouse (1957) experimentally investigated the weir discharge coefficient C_d in (5-1) as a function of H_1/w, where H_1 = the driving head and w = the height of sharp-crested weir.

$$q = C_d \frac{2}{3} \sqrt{\frac{2}{3} g} H_1^{3/2} \tag{5-1}$$

Here, q is the discharge per unit width of the weir, g is the acceleration due to gravity, and H_1 is the total head of the approaching flow measured above the weir crest. Kindsvater and Carter (1957) presented a comprehensive solution for the weir discharge characteristics based on experimental results and dimensional analysis. Rajaratnam and Muralidhar (1971) experimentally determined the detailed distributions of velocity and pressure in the region of the weir crest. Han and Chow (1981) used ideal flow theory and

developed a hodograph model to get some gross characteristics of the flow. Based on experimental results and simplified theoretical considerations, a general relationship between the weir discharge coefficient C_d and the parameter H_1/w was determined by Ramamurthy et al. (1987). Recently, Khan and Steffler (1996) predicted the water surface profiles for sharp-crested weirs with sloping upstream faces, using two-dimensional finite element model involving vertically averaged continuity, longitudinal momentum and vertical momentum equations. For weir slopes up to 27° with the horizontal, their computed results for weir with sloping upstream faces agreed well with test data. For larger upstream weir slopes, numerical instability was encountered. Wu and Rajaratnam (1996) experimentally determined the reduction factor for flow over sharp-crested weirs due to submersion. Martinez et al. (2005) presented the characteristics of compound sharp-crested weirs.

In this chapter, the Reynolds Averaged Navier-Stokes (RANS) equations are applied to solve the problem of flow past a sharp-crested weir in a rectangular open channel. The two-dimensional RNG k-ε turbulence model is adopted for the numerical simulation. The fractional volume of fluid (VOF) method is used. The results of simulation are validated using the experimental (Rajaratnam and Muralidhar 1971, and Ramamurthy et al. 1987) data pertaining to surface profiles and the distributions of velocities and pressure heads.

5.2 Experimental Data

Two sets of experimental data are used to validate the predictions of the turbulence model; the experimental data of Rajaratnam and Muralidhar (1971) and the test data of Ramamurthy et al. (1987).

The experiments of Rajaratnam and Muralidhar (1971) were conducted in two different horizontal rectangular channels. The first channel whose results are used to validate the numerical predictions was 31.1 cm wide and 4.88 m long made by plexiglass plates. The corresponding sharp-crested weir was located at a distance of 0.9 m from the downstream end of the channel. It was made of aluminum and was 29.7 cm high (Fig 5.1). The pressure distribution in the curvilinear regions was measured using a screw-driver static probe (Rajaratnam and Muralidhar 1970). A calibrated pitch probe (Rajaratnam and Muralidhar 1967) was used to measure the velocity distribution in the highly curved regions. Also, the velocity distribution in the regions of negligible curvature was obtained using a Prandtl tube. The flow rate was measured by means of an orifice meter.

Subramanya and Awasthy (1972) used a horizontal rectangular flume 60 cm wide and 6 m long. The sharp-crested weir models (Fig 5.1) were made of plexiglass plates and fixed at the downstream end of the flume. To measure the total pressure head distribution over the weir, a five-hole Pitot sphere (Rae and Pope, 1984) was used. The static pressure distribution in the curvilinear nappe region was measured using a screw-driver static probe (Rajaratnam and Muralidhar 1970). The difference between the total and static pressure heads yielded the velocity head. Also, the flow depth was obtained using a point gage. The discharge was measured using a standard 90° V-notch.

5.3 Solution Procedure

The computational domain is shown in Fig. 5.1. The channel upstream of the weir L_u is 4.88 m long. The channel downstream of the weir L_d is 1.00 m long. The weir is 0.297 m high. Body fitted coordinates are used in the Cartesian frame. The flow domain is meshed

with a power law function that generates a fine mesh in the vicinity of the channel boundary. The grid cells next to the boundary are constructed well within the turbulent region. The results were checked for grid independence using a coarser grid whose cells dimensions were twice as those of the final grid cells sizes. Also, the results were checked using a finer grid whose cells dimensions were half as those of the final grid cells sizes. The results of the coarser grid size were in less agreement than the results related to the final grid. Further, the results for the finer grid were essentially the same as the case of the final grid chosen. The deviations of parameters, velocities and pressures, were generally much less than 1% between the results obtained from the final grid and the finer grid.

Through the time-dependent simulation (for the specified inlet and outlet conditions), the water flows in the open channel and constitutes the free surface between air and water. In the simulation, two different values of H_1/w (0.625 and 6.000) were chosen. These are the same flow parameters as in Experiment number A1 of Rajaratnam and Muralidhar (1971).

The VOF scheme and standard wall functions are used for the free surface boundary and the solid boundaries, respectively (Secs. 2.2.1 and 2.2.2). The depth of flow, average velocity and the quantities of the turbulence are given at the inlet boundary (Fig. 5.1; Sec. 2.2.3). At the outlet (Fig. 5.1) that is enough far away from the weir, water surface obtained using the linear extrapolation method and the gradients of all velocity components and turbulence quantities are zero.

5.4 Results

At the crest section c-c, the finite size of the static and dynamic pressure probes can be expected to cause some interference effects while measuring pressure and velocity. Further, the curvature of the flow near the crest 'c' is high. This may prevent very accurate pressure and velocity measurements there. For flow past a two-dimensional sharp-crested weir at the location of the weir crest c-c (Fig. 5.1), Fig. 5.2 shows the distributions of pressure and velocity as well as the velocity angle ϕ (= Arc tan u_2/u_1). Fig. 5.2a shows the variation of the distribution of the non-dimensional pressure head h/Y_c with x_2/Y_c at the crest section. Here, Y_c = nappe thickness at crest 'c' (Fig.5.1) and x_2 = distance above the crest. In Fig 5.2a, the pressure distribution obtained by the present simulation is compared with the experimental data of Rajaratnam and Muralidhar (1971) and Ramamurthy et al. (1987). In Fig. 5.2b, the non-dimensional axial velocity u_1/U_0 is plotted against the non-dimensional flow depth above the sharp crest x_2/Y_c. Here, the velocity $U_0 = \sqrt{2gH_1}$. The results of the simulation are in generally good agreement with the existing test results. The predicted relation between the velocity angle ϕ and x_2/Y_c based on the test data also appears to follow the trend of the earlier test data (Fig. 5.2c).

Fig. 5.3 shows the distributions of pressure and velocity as well as the velocity angle ϕ at section s-s (Fig. 5.1). As in the previous case, the predicted values of flow parameters are close to the test data.

Fig. 5.4 shows the predicted non-dimensional flow profiles denoting x_2/H_1 as a function of the non-dimensional distance x_1/H_1 for subcritical approach flows. In Fig. 5.4, the surface profiles of the simulation are compared with the experimental profiles

(Rajaratnam and Muralidhar 1971). The two profiles agree well with the present simulated profiles.

Fig. 5.5 shows the variation of the weir parameter $w/(H_1+w)$ with the Froude number Fr_a in the approach channel. It includes a few points related to the present simulation and the previous experimental studies. The agreement between the test data, simulation results and theoretical predictions based on ideal flow theory (Han and Chow 1981) are reasonable (Fig. 5.5).

5.5 Conclusions

The two-dimensional two-equation RNG k-ε turbulence model union with the VOF scheme reproduces faithfully the characteristics of flow past a sharp-crested weir in a rectangular open channel. The predictions of the numerical model agree well with the existing experimental and theoretical results related to water surface profiles and distributions of the pressure head and velocity distributions. Due to the lower time demand and lower cost of numerical methods compared to experimental methods in predicting the flow characteristics, simulation of the sharp-crested weir flows based on a properly validated model provides the weir flow characteristics for various flow configurations encountered in the field.
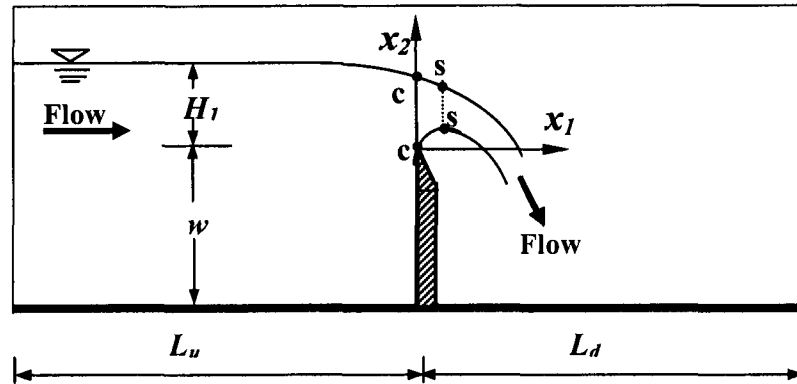
Fig. 5.1 Computation domain for flow past

sharp-crested weirs
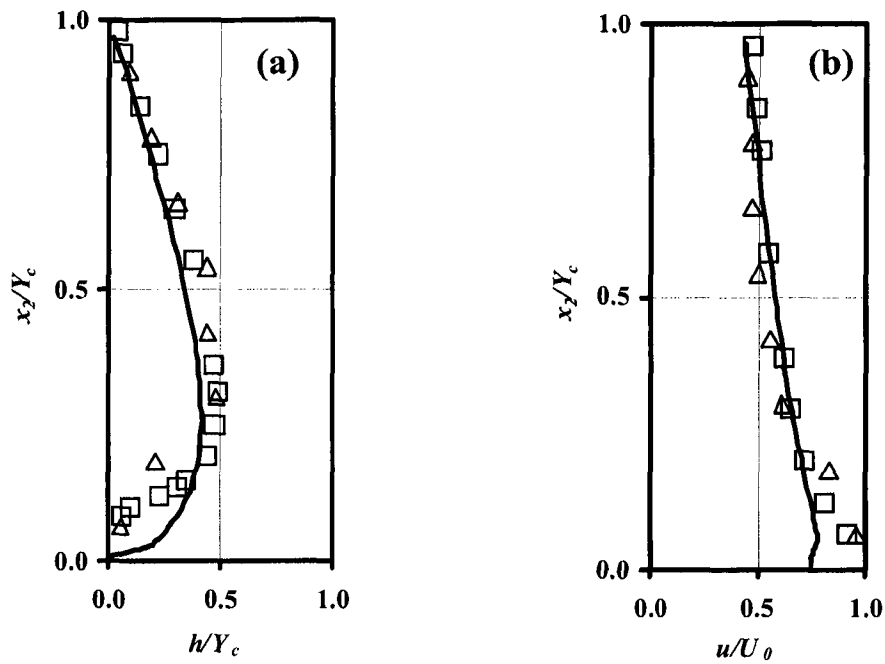
Fig. 5.2 Flow characteristics at section c-c

   a) Pressure distributions

   b) Velocity distributions

   c) Angle of velocity vector

□   Exp. Data (Rajaratnam and Muralidhar, 1971)

Δ   Exp. Data (Ramamurthy et al., 1987)

—— Numerical Simulation ($H_1/w = 0.625$)
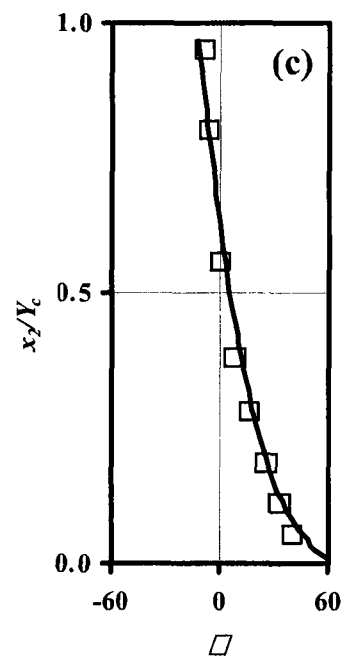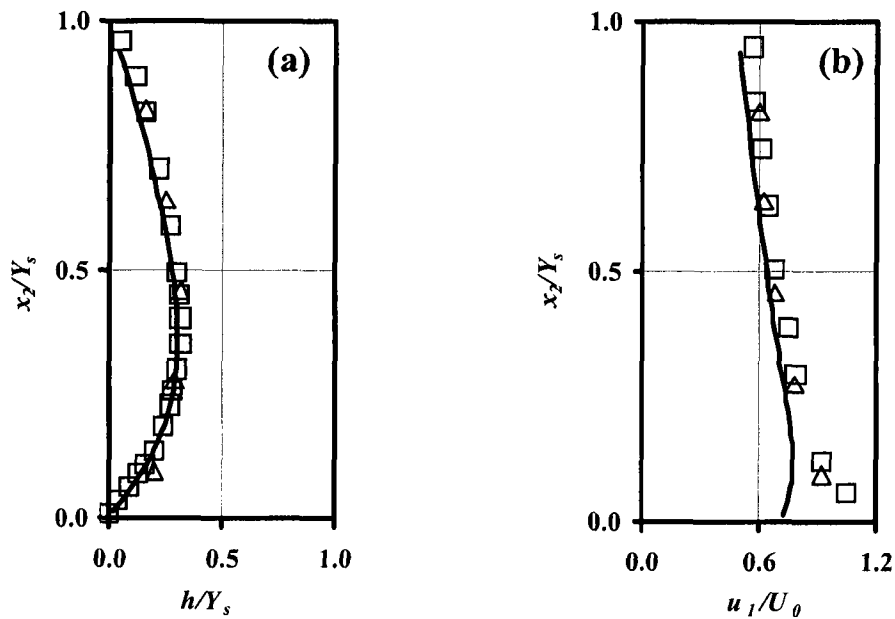
Fig. 5.3 Flow characteristics
at section s-s

a) Pressure distribution

b) Velocity distribution

c) Angle of velocity vector

☐ Exp. Data
(Rajaratnam and Muralidhar, 1971)

△ Exp. Data
(Ramamurthy et al. 1987)

— Present simulation
(H_l/w = 0.625)
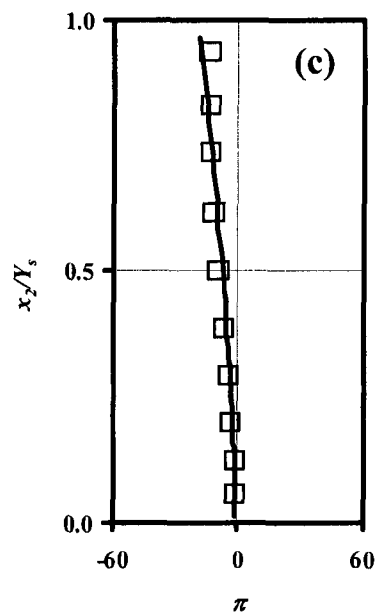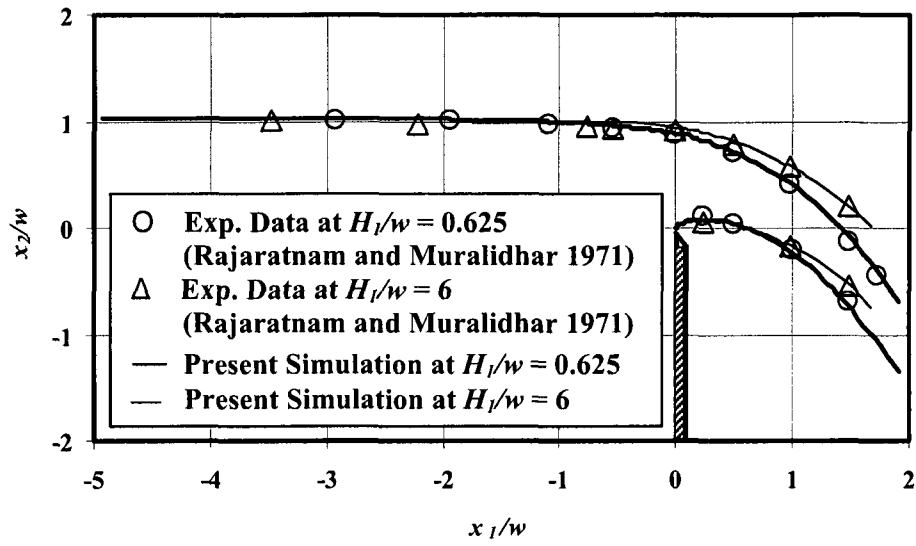
Fig. 5.4 Water surface profiles near the nappe region
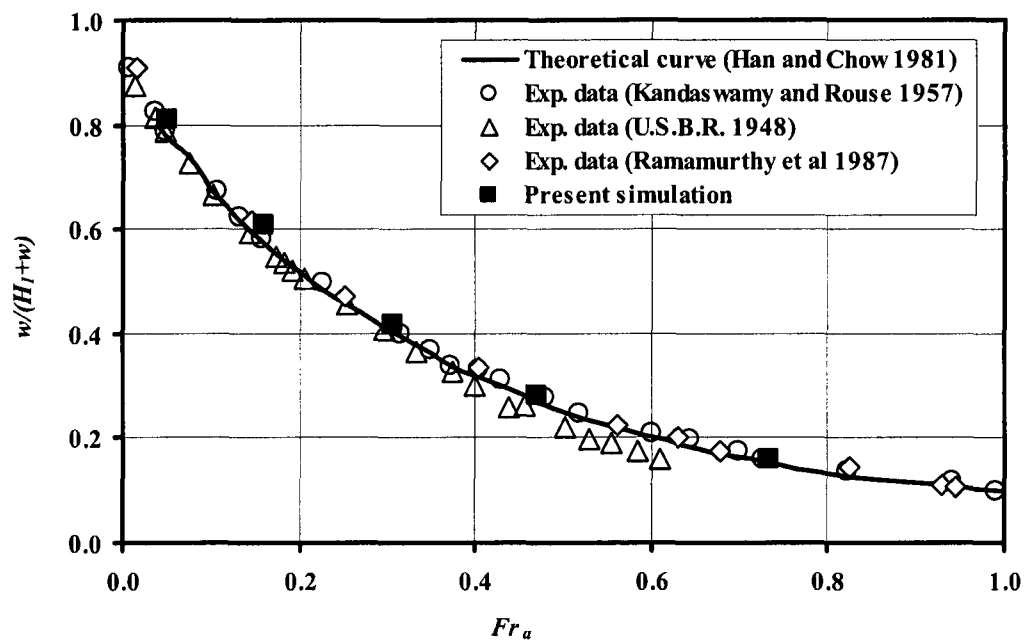
Fig. 5.5 Variation of Weir Parameter $w/(H_1+w)$ **with**

Froude number Fr_a

Chapter 6

Simulation of Flows through Siphon Spillways

6.1 Introduction

A siphon spillway is a closed conduit system formed in the shape of an inverted U (USBR, 1987). The shape of the crest (Fig. 6.1) is usually a circular arc. The level of the air-regulated siphon spillway crest is usually the same as the normal water surface of the upstream reservoir. As the reservoir water surface rises above normal, the initial discharges of the spillway are similar to flow over a weir (free flow). Siphonic action (priming) takes place when the outlet is blocked either by tailwater submergence or by a jet deflector (Fig. 6.1) to stop downstream air accessing the conduit. During the priming, at first air enters the conduit along with water from the entrance (air-regulated or aerated flow). When the water level in the reservoir increases further, the conduit acts as a pipe with no air entrainment that is termed as blackwater flow. More details may be found in USBR (1987) and the studies of Vischer and Hager (1997).

The initial overflow discharges (free flow) are approximately proportional to the 3/2 power of the hydraulic head over the normal level of the reservoir and blackwater flow rate is nearly proportional to the square root of the difference in water heads of the upstream and downstream sections. Fig. 6.2 shows a typical stage-discharge curve for an air-regulated siphon. Once the siphon acts as a pipe, the flow discharge depends on the total head difference between the upstream and downstream reservoirs:

$$q = C_d \, d \sqrt{2g\Delta H} \qquad\qquad (6\text{-}1)$$

Here, q is the discharge per unit width of the spillway, g is the acceleration due to gravity, d is the siphon throat depth, and $\Delta H = H_1 - H_2$. H_1 and H_2 are the total heads of water in downstream and upstream of the structure, respectively. Also, C_d is the discharge coefficient.

In the past, several investigators have studied the characteristics of flow in the siphon spillways. Rousselier and Blanchet (1951) described several realizations of siphon spillways. Head (1971) experimentally studied an air-regulated river siphon model and described its design and operation. Charlton (1971) theoretically studied designing and modeling of the older type and air-regulated siphons. Ackers and Thomas (1975) investigated the operation of several full scale siphons according to the field observations (the siphons were designed with the aid of models). A low-head air-regulated siphon model was studied in detail by Head (1975) to guide the researchers who want to design air-regulated siphon models. Unser (1975) carried out several models to study these kinds of siphons experimentally and presented a relationship between the siphonic discharge and the flow rate of water for the case the siphons act as free overfall weirs. Ali and Pateman (1980) investigate the air-regulated spillways experimentally and theoretically. The full behavior of air-regulated siphon spillways was studied by Ervine and Oliver in 1980. Bollrich (1994) presented the results of his study on a high-head siphon spillway based on the investigation of its rehabilitation. An experimental study was conducted by Houichi et al (2006) on a siphon spillway having the Creager-Ofitserov profile with one to four openings in order to determine their discharge capacities.

The discharge coefficient (C_d) of a circular spillway can be approximately obtained from the empirical general formulas or graphs. Although the discharge coefficient of a circular spillway is affected by the upstream and downstream slopes, upstream depth of flow, and surfaces roughness, it is mainly a function of the ratio of upstream water head to the crest radius. In contrast, no universal graphs or empirical equations can be provided to obtain the discharge coefficients of the siphonic flows through the siphon spillways; because the siphon C_d is influenced by the dimensionless radii of the crest and crown, the form of the entrance, the geometry of the outlet, the depth of tailwater, and the size and position of the nappe deflector. The latter greatly affects the value of C_d. Although the friction losses have an effect on the discharge coefficient of a siphon spillway, the form losses are dominant.

In the present study, the discharge coefficients of the blackwater in the siphon spillways tested experimentally and modeled numerically. The flow in the siphon spillway is highly curvilinear and is also rapidly varied. Turbulence modeling permits one to simulate the flow in a siphon spillway. The isotropic turbulence models are based on the Boussinesq eddy viscosity hypothesis which assumes a linear variation of the components of the Reynolds stress tensor with the mean rate of strain tensor. As such, they cannot correctly predict the characteristics of flows where the streamlines are highly curved (Wilcox 2007). In the present study, the Reynolds Stress Model (RSM) is used to obtain the discharge coefficient of the siphon spillway flow. The two-dimensional finite volume discretization is used for the numerical simulation. Also, the VOF scheme is adopted to model the water surface.

6.2 Experimental Data

A plexiglass siphon spillway model is set in a rectangular channel to test the coefficient of flow discharge through the siphon. The flume and siphon sections are 25.1 cm wide (Fig. 6.1). The depth d of the conduit is 11.1 cm and the radii of the crest and crown are, respectively, 3.7 and 14.7 cm. The sidewalls are made of plexiglass plates for flow visualization. A deflector is set on the bottom face of the lower leg to guarantee that the siphon acts as an air-regulated one when the conduit exit is not completely submerged. Test is performed on the spillway model with different combinations of upstream and downstream water levels. Point gages are used to measure the flow depths upstream and downstream of the spillway. These gages can measure depths to the nearest 0.1 mm. The flow rates are measured using a standard $30°$ V-notch. The accuracy of the discharge measurement is 3%.

In addition to the present test data, the experimental data of Head (1975) are also used to validate the predictions of the turbulence model. Head used a 150 mm wide model (Fig. 6.3) constructed of timber and plastic. The depth d at the conduit crest region is 12.0 cm. The radii of the crest and crown are, respectively, 9.0 and 21.0 cm. In this study, considerable details of the experimental procedure and results are provided to enable one to validate the corresponding numerical simulation.

In Head's model, $\Delta H/d$ ranged from 1 to 2.5. The present model covers a higher range of $\Delta H/d$ from 2 to 6.

6.3 Solution Procedure

The finite volume method with collocated cells arrangement was used to approximate the governing equations to algebraic equations that can be solved numerically. The pressure-velocity coupling scheme was achieved using the PISO algorithm (Pressure-Implicit with Splitting of Operators; Issa, 1986).

The flow domains related to two physical models (Head's model and the present experimental model) were meshed with a power law function that generates the finer mesh close to the solid boundaries. The first grid cell rows next to the solid boundaries were constructed well within the logarithmic region $30 < u_\tau y/v < 100$. The results were checked for grid independence using coarser grids whose cells dimensions were twice as those of the final grids cells sizes. Also, the results were checked using finer grids whose cells dimensions were half as those of the final grids cells sizes. The results of the coarser grids were in less agreement than the results related to the final grids. Further, the results for the finer grids were essentially the same as the case of the final grids chosen. For every model, through the time-dependent simulation, water flows in the siphon system and constitutes the free surface between air and water.

The VOF scheme is used for the free surface boundaries (Sec. 2.2.1). The standard wall functions are used for the solid boundaries (Sec. 2.2.2). For every model, the discharge and the quantities of the turbulence are fixed at the upstream boundary far away from the structure. At the downstream end that is enough far away from the structure, water surface is given. The gradients of all velocity components and turbulence quantities are

zero at the downstream outlet. The total heads at two sections upstream and downstream of the siphon structure are calculated.

6.4 Results

Fig. 6.4 and 6.5 show the comparison of the predicted model results with test data of the present studies and the previous tests (Head, 1975). According to these graphs, there is a good agreement between the numerical predictions and the experimental results. No universal graphs or empirical equations can be provided to obtain the discharge coefficients of the siphonic flows through the siphon spillways. For the reason that the siphon C_d is influenced by the form losses which are determined by dimensionless radius of the crest (R_1/d), the form of the entrance, the geometry of the outlet, the depth of tailwater, and the size and position of the nappe deflector. The latter greatly affects the value of C_d. As such form losses can be reduced by varying the configuration of the entrance, the crest radius, the deflector shape and position, and the outlet geometry. For instance, Head (1975) improved the siphon discharge coefficient by adopting the diffuser shape for the outlet. Although the friction losses have some effect on the discharge coefficient of a siphon spillway, the form losses are dominant.

6.5 Conclusions

The two dimensional RSM along with the VOF scheme can properly predict the discharge coefficient of the blackwater flow through a siphon spillway. The predictions of the numerical model agree well with the experimental results. Simulation of the flows through the siphon spillways based on a properly validated model provides the flow characteristics of these structures for various flow configurations encountered in the field

since numerical modeling demand less time and expense compared to physical modeling

needed to predict the flow characteristics.
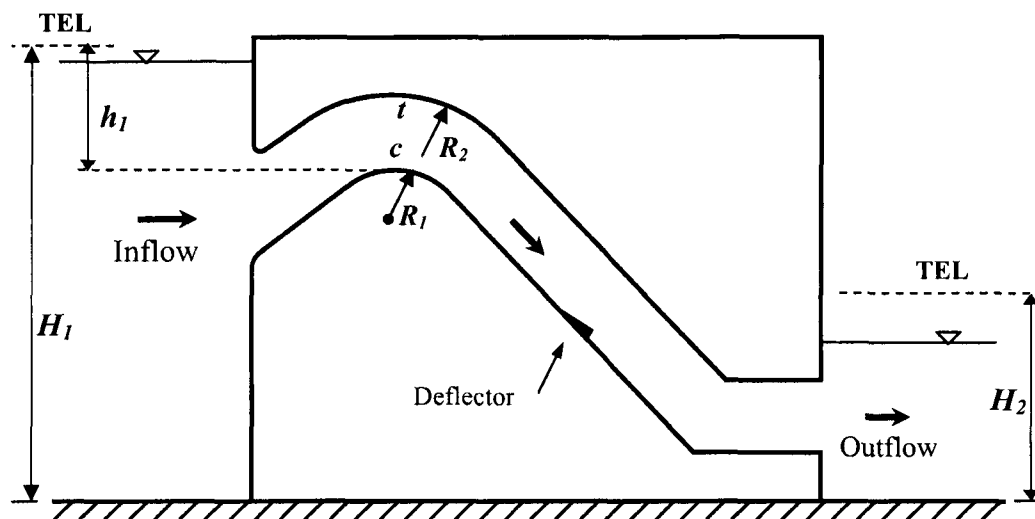
Fig. 6.1. Siphon spillway, longitudinal section
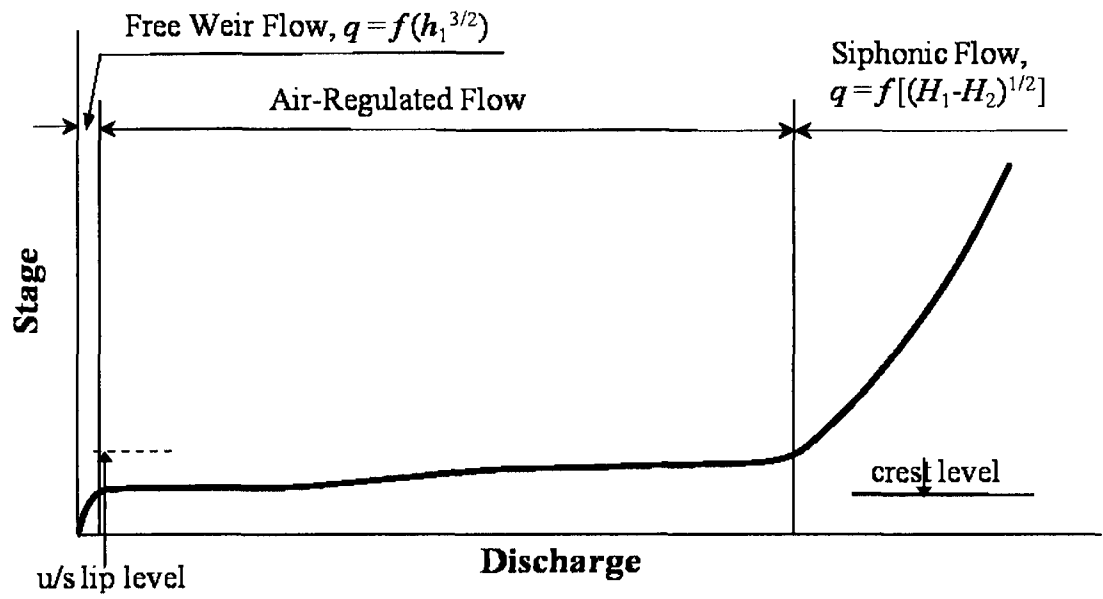
Fig. 6.2. Typical stage-discharge

relationship for a siphon spillway
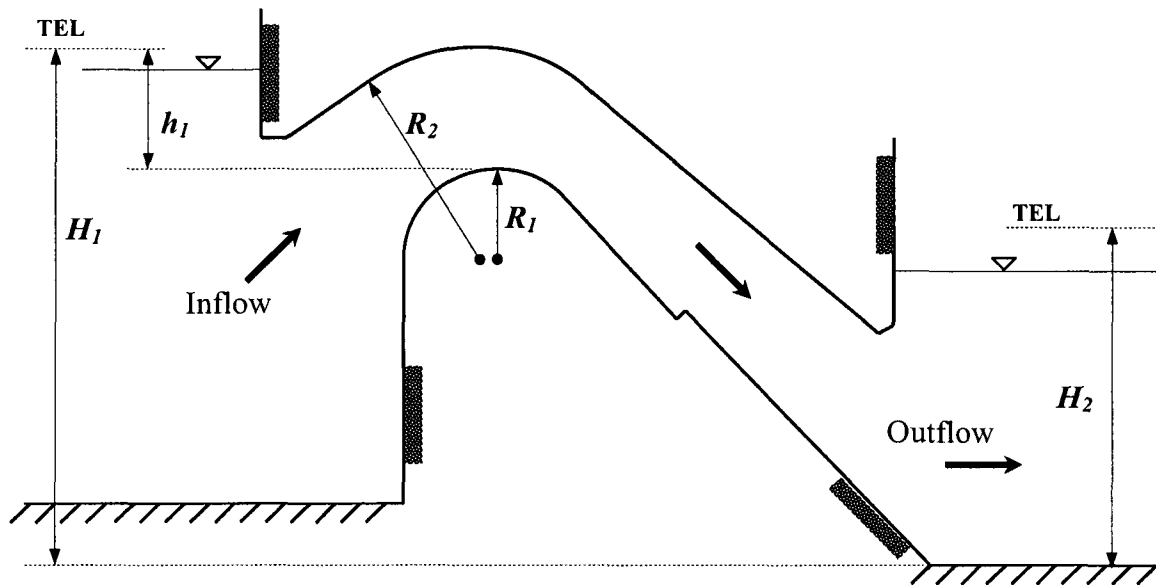
Fig. 6.3. A siphon spillway model

(Head, 1975), longitudinal section
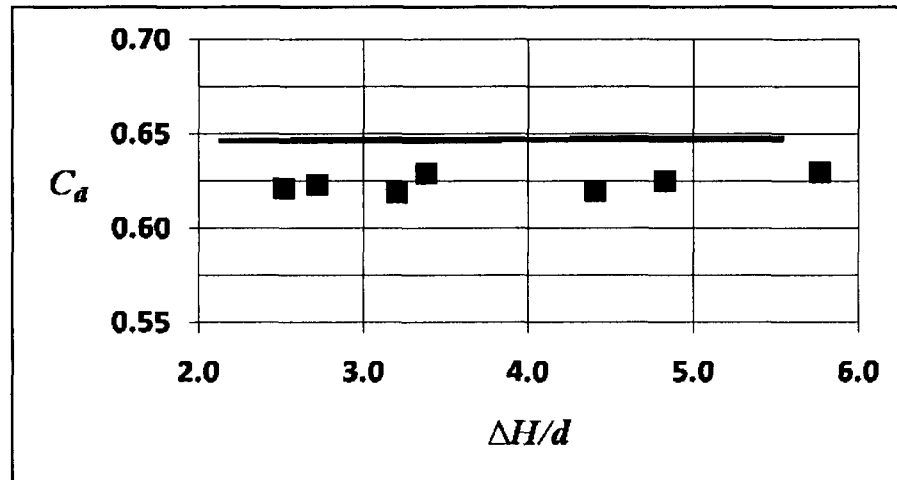
Fig. 6.4. Siphonic discharge; variation of discharge

coefficient with dimensionless head (Fig. 6.1)

— RSM

■ Experimental Data
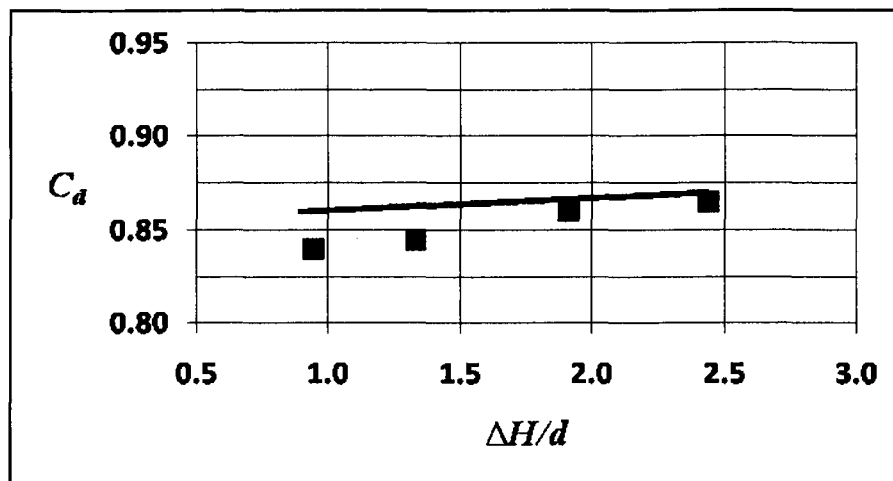
Fig. 6.5. Siphonic discharge; variation of discharge coefficient with dimensionless head (Fig. 6.3)

— RSM

■ Experimental Data (Head, 1975)

Chapter 7

Turbulence Modeling of Flows over Circular Spillways

7.1 Introduction

Circular spillways and circular weirs are used to regulate water levels in flood protection works and irrigation systems as well as flow measurement in hydraulic practice. A circular spillway consists of a circular crest of radius R set tangentially to two upstream and downstream faces (Fig. 7.1). The flow over the circular spillway is highly curvilinear and is also rapidly varied.

Turbulence modeling permits one to simulate the flow over a circular spillway. The isotropic turbulence models are based on the Boussinesq eddy viscosity hypothesis which assumes a linear variation of the components of the Reynolds stress tensor with the mean rate of strain tensor. As such, they can not correctly predict the characteristics of flows where the streamlines are highly curved (Wilcox 2007). In the present study, a Reynolds Stress Model (RSM) and two k-ε models are used to obtain the characteristics of the spillway flow.

In the past, several investigators have studied the characteristics of overflow spillways. Most of them have tried to find the effects of different weir and flow parameters on the discharge coefficient C_d in (7.1), relating the discharge per unit width of the spillway q to

the total head of the approaching flow measured above the spillway crest H_l (Bos, 1989; Chow, 1959; and Chaudhry, 1993).

$$q = C_d \frac{2}{3} \sqrt{\frac{2}{3} g} H_1^{3/2} \tag{7-1}$$

Here, q is the discharge per unit width of the spillway, g is the acceleration due to gravity, and H_l is the total head of the approaching flow measured above the spillway crest.

Jaeger (1956) and Sananes (1957) related the minimum crest surface pressure head with the parameter H_l/R, the dimensionless crest flow depth, and the streamline curvature. R is the radius of the spillway crest. Escande and Sananes (1959) showed that suction of the crest boundary layer increases C_d. Matthew (1963) described a theory that explains the influence of streamline geometry, viscosity, and surface tension on C_d. Cassidy (1965) presented ideal fluid flow models for these spillways. Further, Cassidy (1970) proposed a rational procedure to pass the maximum flow over the standard spillway with a specified minimum crest pressure. Sarginson (1972) showed that the discharge coefficient C_d is slightly greater than unity. Sinniger and Hager (1985) introduced an equation for C_d based on Matthew's theoretical approach (1963). Ramamurthy et al (1992) applied the momentum principle to derive an equation for C_d. Ramamurthy and Vo (1993) adapted Dressler theory to formulate the model for curvilinear flow past circular spillways. An empirical model based on irrotational flow over the circular spillway was also presented in the past (Ramamurthy et al, 1994). Different upstream flow conditions were considered by Chanson and Montes (1998) to indicate that discharge measurements with circular weirs are affected by upstream flow conditions. More recently, Heidarpour and Chamani (2006) studied the characteristics of the flow past circular spillways based on

potential flow theory. They provided a simple method to determine the velocity distribution on the spillway crest. Also, they were able to relate the spillway discharge coefficient with the total head of the approach flow and the crest radius.

In this chapter, a comparative study of three different turbulence models (RSM, RNG k-ε, and Standard k-ε models) was made to analyze the characteristics of the flow over circular spillways. The two-dimensional finite volume discretization was used for the numerical simulation. Also, the VOF scheme was adopted to model the water surface. The experimental data related to spillway flows of Vo (1992) and Heidarpour and Chamani (2006) were used to validate the results.

7.2 Experimental Data

Two sets of experimental data are used to validate the predictions of the turbulence models; the experimental data of Vo (1992) and the test data of Heidarpour and Chamani (2006).

Vo (1992) used a few plexiglass weir models with different crest radii in a rectangular channel. The test section was 25.4 cm wide. The sidewalls were equipped with transparent windows for flow visualization. Test performed on spillway models with combinations of upstream slopes α and downstream slopes β (Fig. 7.1). Sufficient pressure taps of diameter 0.5 mm were installed for the models to record the pressure distributions along the centerline of the models on the spillway crests and the upstream wall faces. Point gages were used to measure the flow depths upstream of the spillways. The flow rates were measured using a standard 60° V-notch. Also, a Laser Doppler

Velocimeter (LDV) system was used to survey the horizontal velocity distribution above the spillway crests. In the present study, the experimental results of the model with R = 15.2 cm are used. The corresponding values of L_a and w (Fig. 7.1) from the experiments of Vo (1992) were 1.80 and 1.16 m, respectively. Other parameters of the six tests that are used for validation are given in Table 7.1.

Heidarpour and Chamani (2006) were set their circular spillways in a smoothed rectangular flume with a 32 cm wide section. The test that was considered for validation of numerical predictions had $\alpha = 90°$, $\beta = 90°$, $w/R = 3$, and $H_l/R = 1.06$ (Fig. 7.1). They measured the discharges by a volume-to-time method. The flow depths were obtained using point gages. Also, a Prandtl-Pitot tube was used to measure the horizontal velocity values over the crest.

7.3 Solution Procedure

The finite volume method with collocated cells arrangement was used to approximate the governing equations to algebraic equations that can be solved numerically. The pressure-velocity coupling scheme was achieved using the PISO algorithm (Pressure-Implicit with Splitting of Operators; Issa, 1986).

The computational domain for the numerical simulation is shown in Fig. 7.1. The earlier tests (Vo, 1992; Heidarpour and Chamani, 2006) were used to validate the numerical predictions. The corresponding values of L_a, R and w (Fig. 7.1) from the experiments of Vo (1992) were 1.80, 0.152 and 1.164 m, respectively. Other parameters of the six tests done by Vo (1992) are given in Table 7.1. To compare the numerical results with the

experimental data of Heidarpour and Chamani (2006), a test was considered with $w/R = 3$, $H_l/R = 1.06$, $\alpha = 90°$, and $\beta = 90°$. The flow domain was meshed with a power law function that generates the finer mesh close to the solid boundaries. The first grid cell rows next to the walls were constructed well within the logarithmic region $30 < u_\tau y/v < 100$. The results were checked for grid independence using a coarser grid whose cells dimensions were twice as those of the final grid cells sizes. Also, the results were checked using a finer grid whose cells dimensions were half as those of the final grid cells sizes. The results of the coarser grid size were in less agreement than the results related to the final grid. Further, the results for the finer grid were essentially the same as the case of the final grid chosen. Through the time-dependent simulation, water flows in the spillway system and constitutes the free surface between air and water.

The VOF scheme is used for the free surface boundary (Sec. 2.2.1). The standard wall functions are used for the solid boundaries (Sec. 2.2.2). According to the experimental models, the depth of flow, average velocity and the quantities of the turbulence are known at the inlet boundary (Fig. 7.1; Sec. 2.2.3). At the outlet (Fig. 7.1) water surface, velocity components and turbulence quantities obtained using the linear extrapolation method.

7.4 Results

Existing experimental results (Heidarpour and Chamani, 2006; Vo, 1992) related to water surface profiles, pressure distributions, and streamwise velocity distributions for flow over the circular spillways were used to validate the numerical simulation predictions. For water surface profiles over the crest, Fig. 7.2 shows that there is a good agreement

between RSM predictions and experimental results. The predictions of the k- ε models for the water surface profiles were essentially within 2% of the predictions of RSM. For clarity, only RSM data are shown in Fig 7.2.

Both experimental and predicted pressure head distributions along the vertical sections at the crests are shown in Fig 7.3. The experimental pressure head obtained very near to the spillway crest boundary by the flat static pressure probe is subject to slight errors due to the high curvature of the flow and the proximately of the solid boundary. This may in part be the reason for the deviation of the data from the model predictions. In general, RSM results agree well with the experimental data.

Fig. 7.4 displays the agreement between RSM and experimental results of the pressure distribution on the upstream wall. The vertical distributions of the streamwise velocities at the crests are presented in Fig. 7.5. The maximum discrepancy of RSM prediction was about 4% where the streamlines have the maximum curvature close to the crest. Fig. 7.6 compares the predictions of the RMS with the recent experimental data of Heidarpour and Chamani (2006) related to the velocity distribution at the crest section of the circular spillway. The agreement appears to be very good between model predictions and the experimental data.

To verify the fact that RSM is superior to Standard k- ε and RNG k- ε in predicting the spillway flow characteristics involving highly curvilinear flows, the test results of the velocity distribution at the spillway crest obtained by Vo (1992) are compared with the predictions of these three models. Fig 7.7 shows that the Standard k- ε model fails to provide the velocity distribution at the spillway crest. However, the RNG k- ε model

properly predicts the velocity except in the region very close to the crest boundary. The corresponding error is of the order of 7%. In equation (2.17) in section 2.1.2, the coefficient $C_{\varepsilon 2}$ is constant (= 1.92) for the Standard k-ε model, while this coefficient is a function of the strain for the RNG k-ε model. This is important for flows subjected to high distortion and therefore improves the predictions of the characteristics of flows in curved geometries modeled by the RNG k-ε model as compared to the Standard k-ε model. The sketch (Fig. 7.7) indicates that the difference between the experimental data and the predictions of RSM is the order of 4% which is acceptable for engineering applications. This better agreement may be traced in part to the ability of RSM to accommodate curvilinear streamlines present near the spillway crest. As stated earlier, for the spillway flow which is highly curvilinear and rapidly varied, unlike the k-ε models, RSM does not assume a linear variation of the components of the Reynolds stress tensor with the mean rate of strain tensor. As such, where the streamlines are highly curvilinear, they can more correctly predict the flow characteristics including velocity distribution.

Fig. 7.8 shows the pressure head distributions at the spillway crest predicted by the three models and the corresponding experimental data (Vo, 1992). For the RNG k- ε model and RSM, the agreement is reasonable between the predictions and test data. However, the predictions of the pressure head distribution at the spillway crest for the Standard k-ε model is poor. This is understandable, since pressure head in curvilinear flows involves a correction term that is proportional to the square of the velocity vector. Since the Standard k-ε model fails to yield a reasonable prediction of the velocity data, it should not be expected to provide accurate pressure head data.

7.5 Conclusions

The Reynolds-Stress Model (RSM) of turbulence along with the VOF scheme enables one to obtain reasonably accurate characteristics of flow over circular spillways which involve highly curvilinear streamlines. The predictions of RSM agree well with the existing experimental results related to the water surface profiles and the velocity and pressure distributions at the crest. Lower time demand and lower cost are associated with numerical methods. As such, simulation of the flows over these spillways based on a properly validated numerical model provides a simple procedure to determine the flow characteristics of the spillways, for various flow configurations that one encounters in engineering practice, without recourse to expensive experimental procedures.
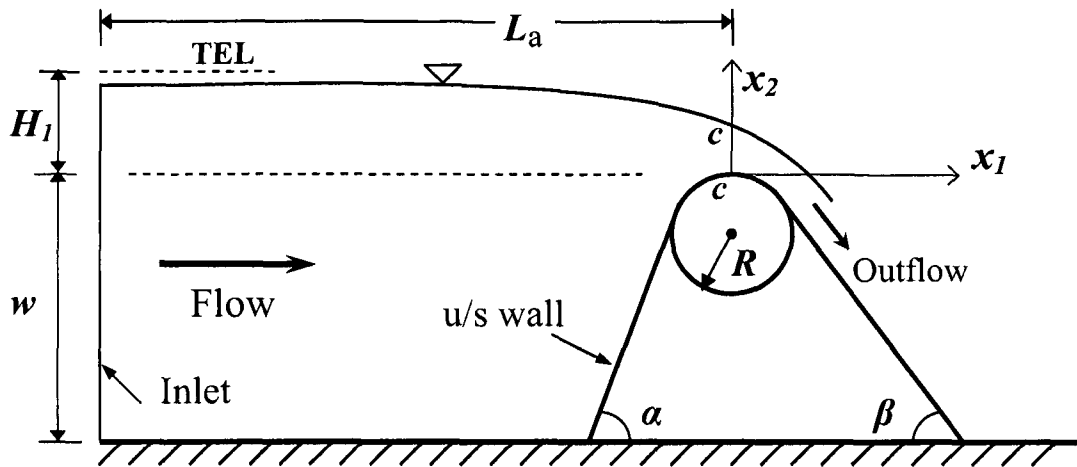
Fig. 7.1. Circular Spillway (computational domain)
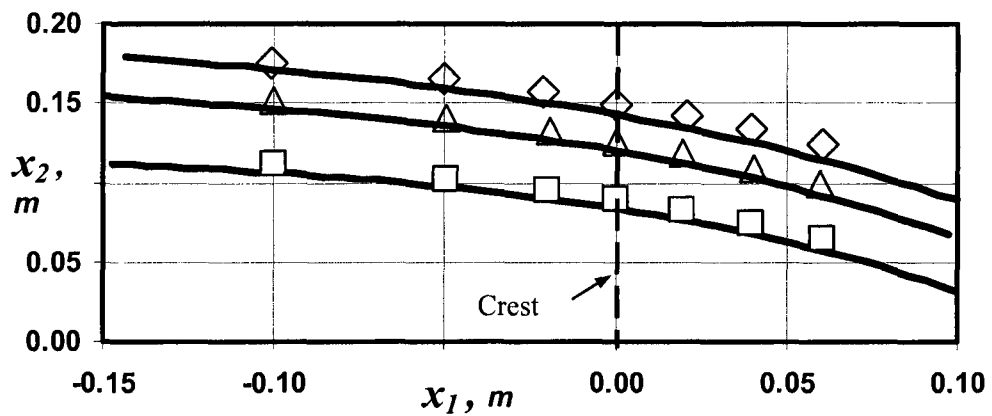
Fig. 7.2. Water surface profiles over the crests

— RSM

Exp. Data (Vo, 1992): □ T1, △ T2, ◊ T3
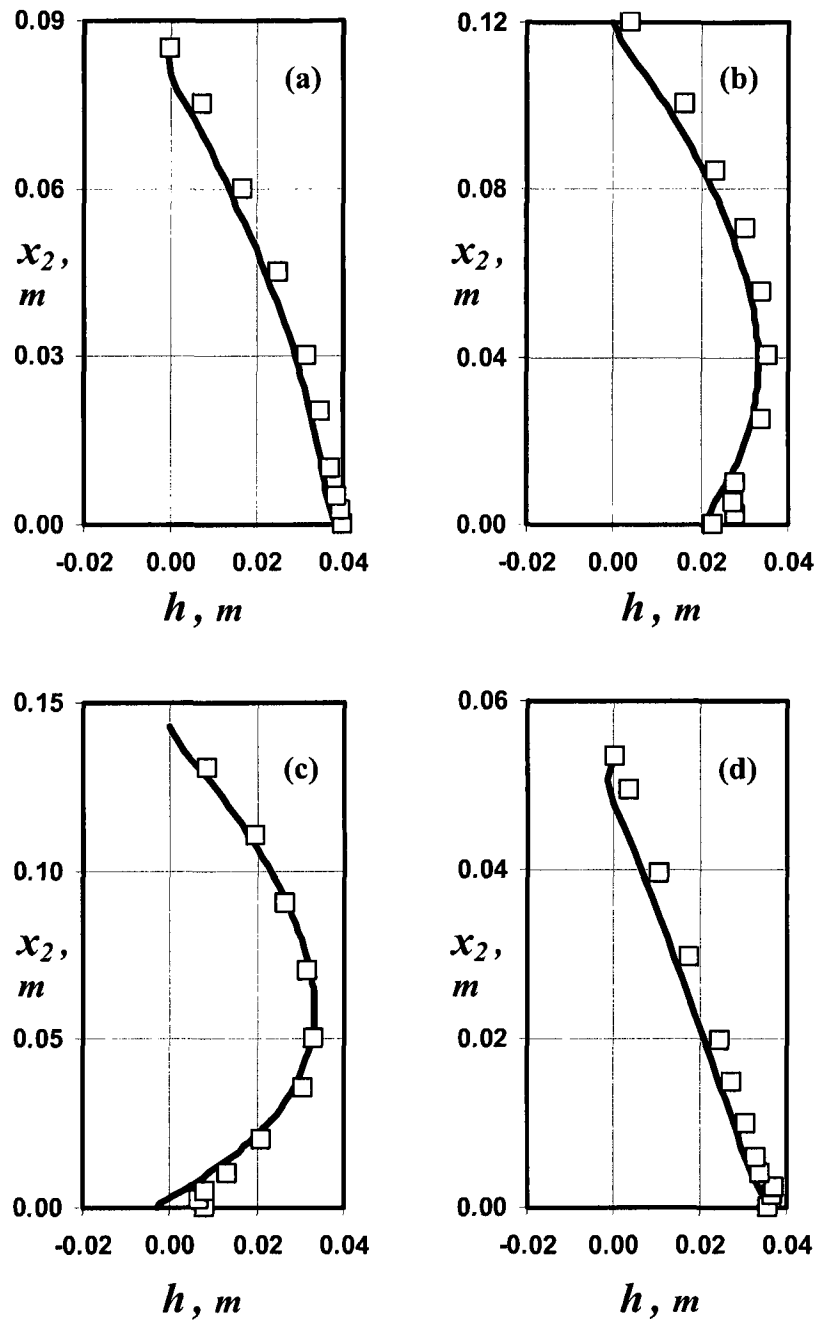
Fig. 7.3. Pressure head distributions at the crests of the spillways

— RSM

□ Exp. Data (Vo, 1992): a) T1, b) T2, c) T3,
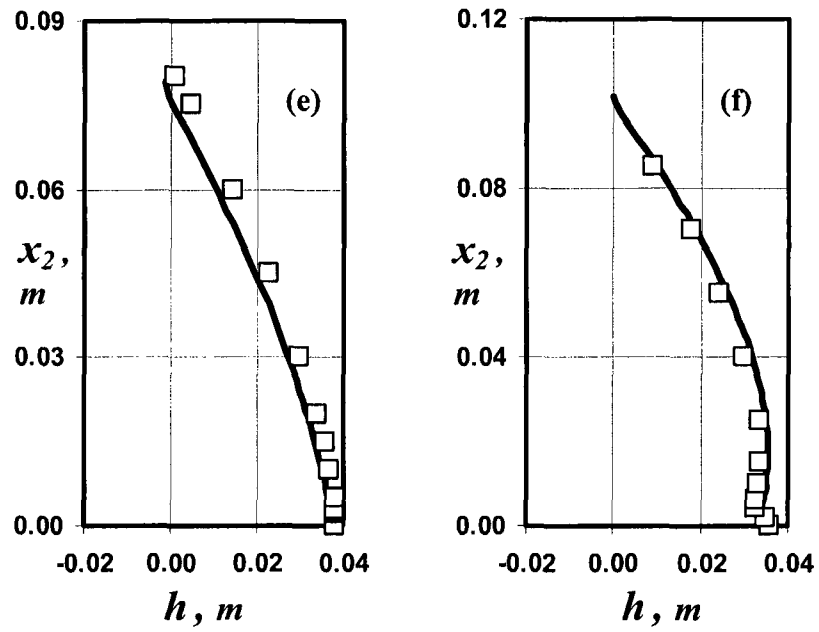
   d) T4, e) T5, and f) T6

Fig. 7.3. (cont.) Pressure head distributions at the crests of the spillways

— RSM

□ Exp. Data (Vo, 1992): a) T1, b) T2, c) T3,
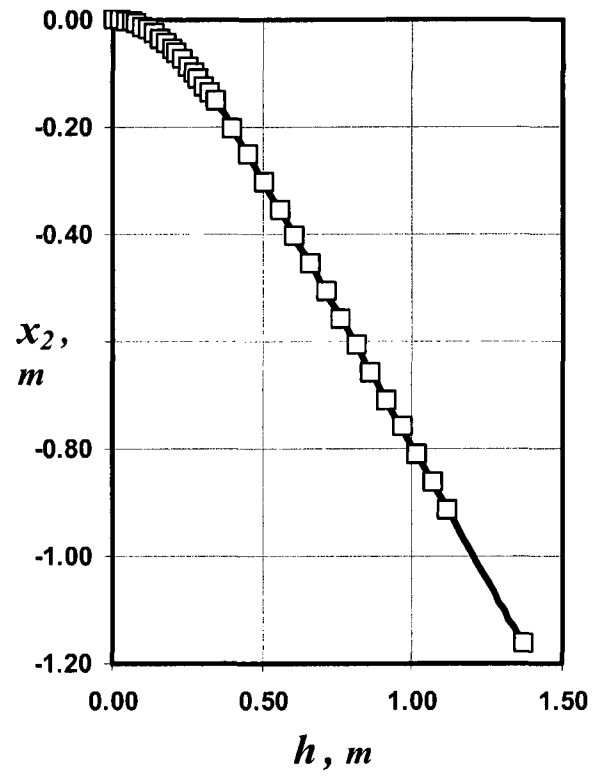
d) T4, e) T5, and f) T6

Fig. 7.4. Pressure head distributions on the upstream wall face

— RSM, □ Exp. Data (Ref. Vo, 1992), T3
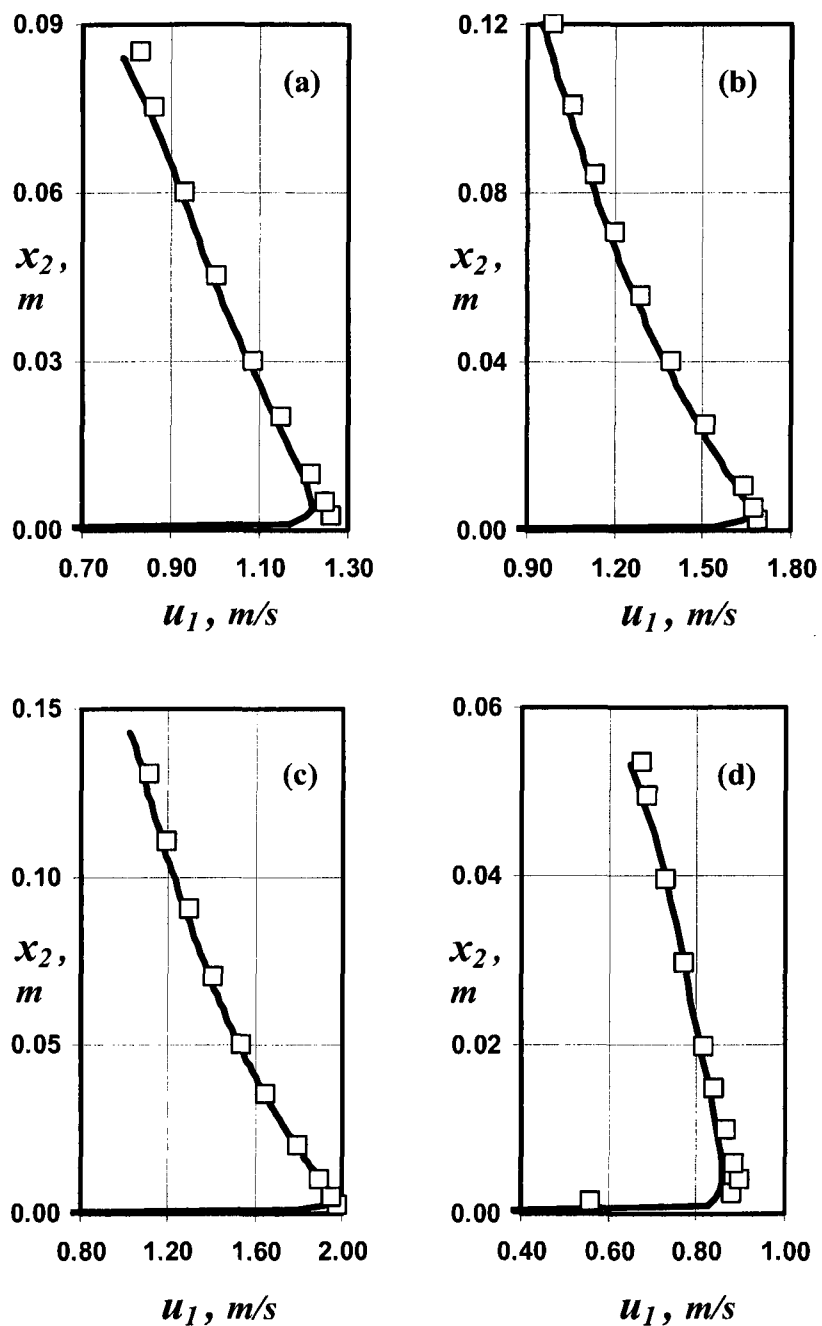
Fig. 7.5. Horizontal velocity distributions at the
crests of the spillways

— RSM

□ Exp. Data (Vo, 1992): a) T1, b) T2, c) T3,
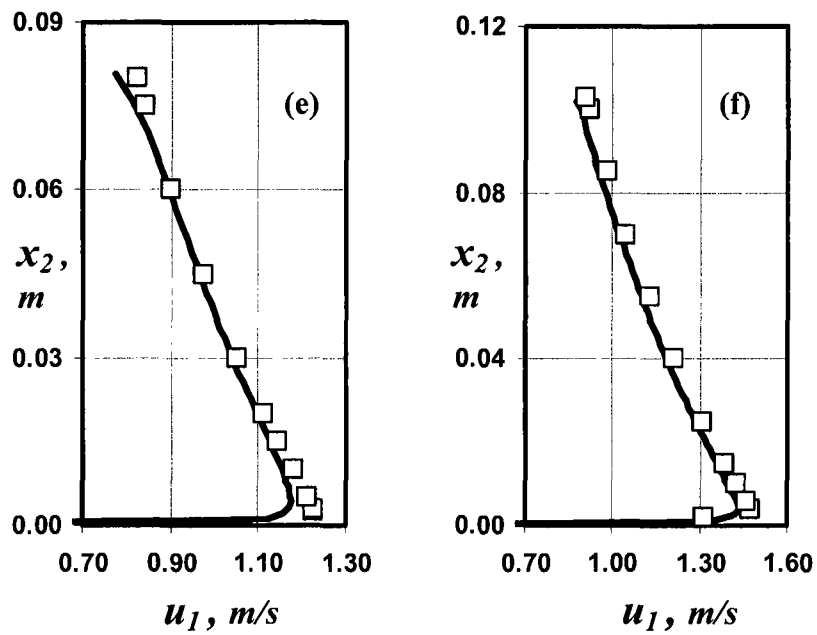
d) T4, e) T5, and f) T6

Fig. 7.5. (cont.) Horizontal velocity distributions at the crests of the spillways

— RSM

□ Exp. Data (Vo, 1992): a) T1, b) T2, c) T3,

d) T4, e) T5, and f) T6
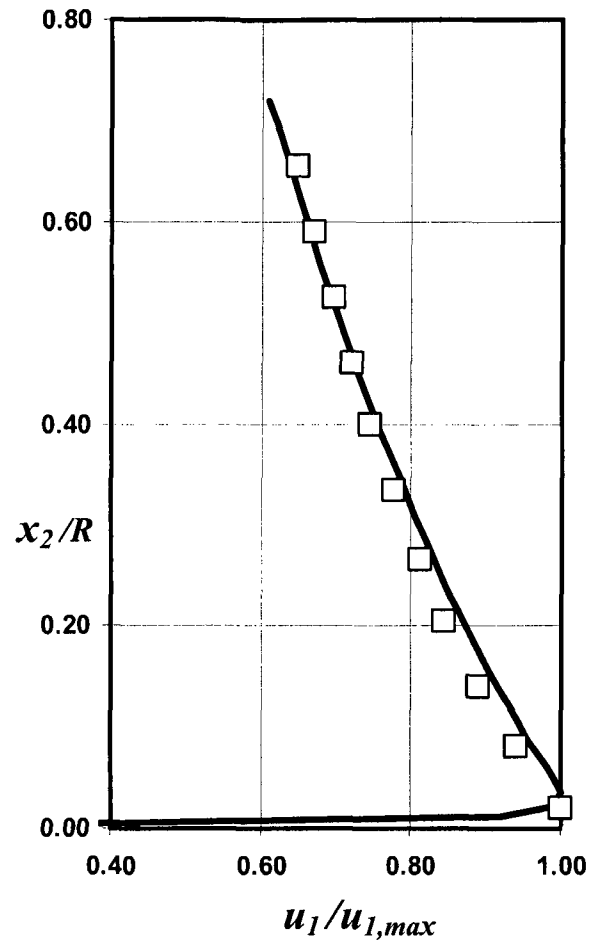
Fig. 7.6 Horizontal dimensionless velocity

distributions at the crest of the spillway

—   RSM

□   Exp. Data (Heidarpour and Chamani, 2006)
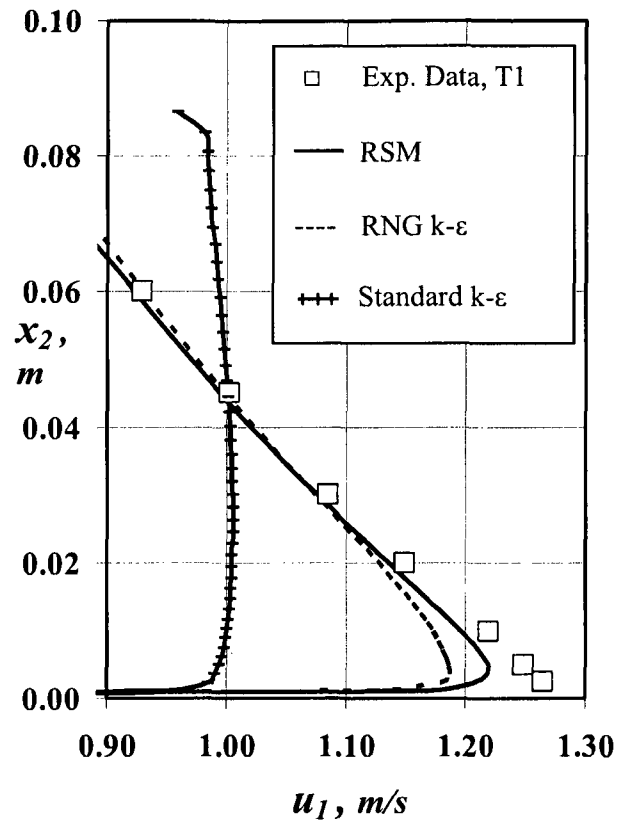
Fig. 7.7. Horizontal velocity distributions at the crest of the spillway (RSM vs. k-ε)
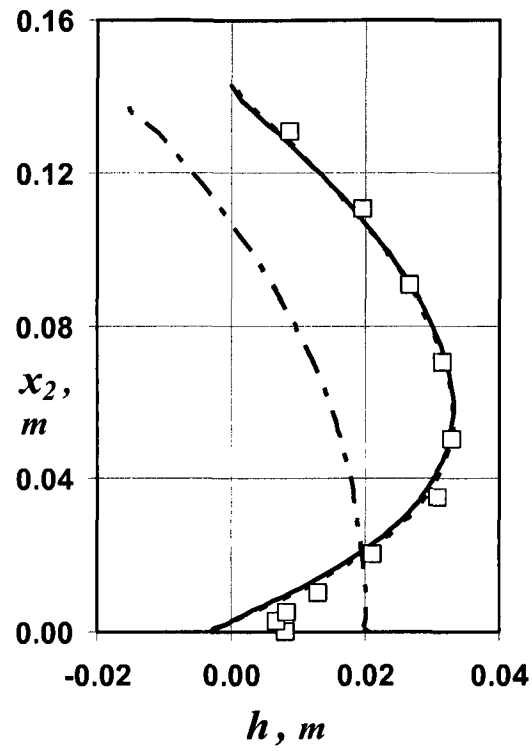
Fig. 7.8. Pressure head distributions

at the spillway crest (RSM vs. k-ε)

□ **Exp. Data, T3 (Vo, 1992),** —— **RSM,**

— · — **Standard k-ε,** - - - **RNG k-ε.**

Test	α (deg.)	β (deg.)	H_l (m)	q (L/s/m)
T1	90	90	0.1237	85.39
T2	90	90	0.1762	152.17
T3	90	90	0.2093	203.43
T4	60	45	0.0796	41.34
T5	60	45	0.1185	80.04
T6	60	45	0.1482	115.71

Table 7.1. Selected experimental

parameters (Fig. 7.1; Vo, 1992)

Chapter 8

Summary, Conclusions and Future Studies

8.1 Summary

In the present study, highly curvilinear flows in several common hydraulic structures were simulated using turbulence modeling. The RANS equations along with turbulence transport equations were modeled using three turbulence models (Standard k- ε model, RNG k- ε model, and RSM). FVM as a discretization technique was used to convert the partial differential equations to the algebraic equations. VOF technique was adopted to find the free surface profiles in the structures. The mean flow characteristics including water surface profiles, pressure distributions, velocity distributions, secondary flows, and discharge coefficients were obtained. To validate the numerical predictions the existing results and results based on the present studies were used. Cut-throat flumes, sharp-crested weirs, side weirs, siphon spillways, and circular spillways were selected for numerical modeling as they are typical flow measuring or regulating hydraulic structures which involve highly curvilinear flows.

Numerical simulation was chosen as the means to study highly curvilinear flows in the hydraulic structures stated above because they are cost effective and yield reliable predictions of flow characteristics especially when a good model is developed and validated properly using the existing test data. This is based on the fact that unlike physical models, it is far simpler to apply changing boundary conditions and flow parameters to a solved numerical model and obtain a flow characteristics for hydraulic

structures associated with highly curvilinear flows. For instance, for a typical spillway, the upstream and downstream boundary conditions (inflow and outflow) may get altered due to modifications in the river system.

8.2 Conclusions

The following conclusions are drawn on the based on the present study. Reynolds Stress Model (RSM), as an accurate and efficient turbulence model, can be used to predict the mean characteristics of highly curvilinear flows in hydraulic structures. These flow characteristics include the water surface profiles, discharge coefficients, pressure distributions, streamwise velocity distributions, and secondary flows. Cut-throat flumes and sharp-crested weirs that are two common flow measurement structures are modeled in the present study. Lateral weirs, siphon spillways, and circular spillways that are typical flow regulation structures are also numerically simulated. The experimental data of existing tests as well as two presently tested models in the laboratory validated the numerical predictions. Due to lower time demand and lower costs associated with the numerical simulation compared to the experimental modeling, numerical simulation of a hydraulic structure involving highly curvilinear flow based on a properly validated model provides a simple procedure to determine the flow characteristics. Without recourse to expensive experimental procedures, the same model can be used to obtain the flow features in the hydraulic structures for various flow configurations encountered in engineering practice.

8.3 Future Studies

1) Reynolds Stress Model (RSM) may be used to predict the wall shear stress in the hydraulic structures. If validated, RSM can help an engineer to improve the design to prevent the structure from severe erosion and sedimentation.

2) In some hydraulic structures, the separation zones are considerable. RSM may be used to obtain the characteristics of separation including its starting and reattaching points and its variable width as well as the flow pattern in this region. Maybe, a Large Eddy Simulation (LES) is more suitable for this application.

3) The approach suggested in this investigation can be extended to other hydraulic structures such as broad-crested weirs, transitions, and shaft spillways.

References

1. Ackers, P., White, W. R., Perkins, J. A., and Harrison, A. J. M. (1978). "Weirs and Flumes", *Wiley*, U.K.

2. Ackers, P. and Thomas, A. R. (1975). "Design and operation of air-regulated siphons for reservoir and head-water control", *Symposium on the Design and Operation of Siphons and Siphon Spillways, BHRA Fluid Engineering*, U.K., A1.1-A1.20.

3. Ali, K. and Pateman, D. (1980). "Theoretical and experimental investigation of air-regulated siphons", *Proceeding of the institution of Civil Engineers, Part 2*, 69, 111-138.

4. Aukle, D. A. (1983). "Free flow discharge characteristics of throatless flumes", M. Eng. Thesis, *Concordia University,* Montreal, Canada.

5. Bates, P. D., Lane, S. N., and Ferguson R. I. (2005). "Computational fluid dynamics: applications in environmental hydraulics", *John Wiley*, Hoboken, N.J.

6. Bollrich, G. (1994). "Hydraulic investigations of the high-head siphon spillway of Burgkhammer", *ICOLD 18th Congress*, South Africa.

7. Borghei, S. M., Jalali, M. R., and Ghodsian, M. (1999). "Discharge coefficient for sharp-crested side weirs in subcritical flow", *Journal of Hydraulic Engineering,* ASCE, 125(10), 1051-1056.

8. Bos, M. G. (1989). "Discharge Measurement Structures", *International Institute for Land Reclamation and Improvement,* Wageningen, the Netherlands.

9. Bureau of Reclamation, (1948). "Studies of Crests for Overall Dams," U.S.B.R. Bulletin 3, Part IV, Boulder Canyon Project Final Reports.

10. Bureau of Reclamation (1987). "Design of Small Dams", 3rd edition, USBR, Colorado.

11. Cassidy, J. J. (1965). "Irrotational flow over spillways of finite height", *Journal of Engineering Mechanics Division, ASCE*, 91 (6), 155-173.

12. Cassidy, J. J. (1970). "Designing spillway crests for high head operation", *Journal of Hydraulic Division, ASCE*, 96 (3), 745-753.

13. Chanson, H. and Montes, J. S. (1998). "Overflow characteristics of circular weirs: effects of inflow conditions", *Journal of Irrigation and Drainage Engineering, ASCE*, 124 (3), 152-162.

14. Charlton, J. A. (1971). "The design of air-regulated spillway siphons", *Journal of the Institution of Water Engineers*, 25, 325-336.

15. Chaudhry, M. H. (1993). "Open-Channel Flow", *Prentice Hall*, Englewood Cliffs, New Jersey.

16. Chen, Q., Dai, G. and Liu, H. (2002). "Volume of fluid model for turbulence numerical simulation of stepped spillway overflow of plane free overfall," *Journal of Hydraulic Engineering, ASCE*, 128(7), 683-688.

17. Chow, V. T. (1959). "Open-Channel Hydraulics", *McGraw-Hill, Inc.,* New York.

18. De Marchi, G. (1934). "Saggio di teoria di funzionamente degli stramazzi laterali", *L'Energia Elettrica.*, 11, 849-860 (in Italian).

19. Ervine, D. A. and Oliver, G. C. S. (1980). "The full scale behavior of air-regulated siphon spillways", *Proceeding of the institution of Civil Engineers, Part 2*, 61, 383-400.

20. Escande, L. and Sananes, F. (1959). "Etude des seuils deversants a fente aspiratrice", *La Houille Blanche,* Grenoble, France, 14 (Spl B), 892-902 (in French).

21. Ferziger, J. H. and Peric, M. (2002). "Computational Methods for Fluid Dynamics," 3rd edition, *Springer-Verlag Berlin Heidelberg,* New York.

22. Hager, W. H. (1982). "Die hydraulik von verteilkanalen", Teil 1-2, Mitteilungen der versuchanstalt fur wassebau, *Hydrologie und Glaziologie,* No. 55-56 (in German).

23. Hager, W. H. (1987). "Lateral outflow over side weirs", *Journal of Hydraulic Engineering,* ASCE, 113(4), 491-504.

24. Han, T.Y. and Chow, W.L. (1981). "The study of sluice gate and sharp-crested weir through hodograph transformations," *Journal of Applied Mechanics, ASCE,* 48(6), 229-238.

25. Head, C. R. (1971). "A self-regulating river siphon", *Journal of the Institution of Water Engineers*, 25, 63-72.

26. Head, C. R. (1975). "Low-head air-regulated siphons", *Journal of the Hydraulics Division, ASCE*, 101(3), 329-345.

27. Heidarpour, M. and Chamani, M.R. (2006). "Velocity distribution over cylindrical weirs", *Journal of Hydraulic Research,* 44(5), 708-711.

28. Houchi, L., Ibrahim, G., and Achour, B. (2006). "Experiments for the discharge capacity of the siphon spillway having the Creager-Ofitserov profile", *International Journal of Fluid Mechanics Research*, 33(5), 395-406.

29. Issa, R. I. (1986). "Solution of the implicitly discretized fluid flow equations by operator-splitting," *Journal of Computational Physics*, 62, 40–65.

30. Jaeger, C. (1956). "Engineering Fluid Mechanics", *Blackie & Son Limited,* Glasgow, U.K.

31. Kandaswamy, P. K. and Rouse, H. (1957). "Characteristics of flow over terminal weirs and sills", *Journal of the Hydraulics Division, ASCE*, 83(4), 11-32.

32. Keller, R. J. (1981). "Scale effect in model studies of cut-throat flumes", *XIX International Association of Hydraulic Research Congress*, New Delhi, India, 4, 40-47.

33. Keller, R. J. (1984). "Cut-throat flume characteristics", *Journal of Hydraulic Division*, 110(9), 1248-1263.

34. Keller, R. J. and Mabbett, G. O. (1987). "Model calibration of a prototype cut-throat flume", *Journal of Hydraulic Research*, 25(3), 329-339.

35. Khan, A.A. and Steffler, P.M. (1996). "Modeling overfalls using vertically averaged and moment equations", *Journal of Hydraulic Engineering, ASCE*, 122(7), 397-402.

36. Kindsvater, C. E. and Carter, R. (1957). "Discharge characteristics of rectangular thin-plate weirs," *Journal of the Hydraulics Division, ASCE*, 83(3), 1353-1-36.

37. Launder, B. E. and Spalding, D. B. (1974). "The numerical computation of turbulent flows", *Computer Methods in Applied Mechanics and Engineering*, 3, 269-289.

38. Launder, B. E., Reece, G. J., and Rodi, W. (1975). "Progress in the development of a Reynolds-stress turbulence closure", *Journal of Fluid Mechanics*, 68(3), 537-566.

39. Launder, B. E. (1992). "Fifth biennial Colloquium on computational fluid dynamics", *Manchester Institute of Science and Technology*, England.

40. Launder, B. E. and Li, S. P. (1994). "On the elimination of wall-topography parameters from second-moment closure", *Physics of Fluids*, 6, 999-1006.

41. Maronnier, V., Picasso, M. and Rappaz, J. (2003). "Numerical simulation of three-dimensional free surface flows," *International Journal for Numerical Methods in Fluids*, 42, 697-716.

42. Martinez, J., Reca, J., Morillas, M. T. and Lopez, J. G. (2005). "Design and calibration of a compound sharp-crested weir," *Journal of Hydraulic Engineering, ASCE*, 131(2), 112-116.

43. Matthew. G. D. (1963). "On the influence of curvature, surface tension and viscosity on flow over round-crested weirs", *Proceedings of the Institution of Civil Engineers,* London, England, 25, 511-524.

44. Meselhe, E. A., Sotiropoulos, F. and Patel, V. C. (1995). "Three-dimensional numerical model for open-channels", *Proceedings of the International Conference on Hydropower – Waterpower, ASCE*, San Francisco, CA, 3, 2315-2324.

45. Mohapatra, P. K., Bhallamudi, S. M. and Eswaran, V. (2001). "Numerical study of flows with multiple free surfaces," *International Journal for Numerical Methods in Fluids*, 36, 165–184.

46. Muslu, Y. (2001). "Numerical analysis for lateral weir flow", *Journal of Irrigation and Drainage Engineering, ASCE*, 127(4), 246–253.

47. Muslu, Y., Tozluk, H., and Yuksel, E. (2003). "Effect of lateral water surface profile on side weir discharge", *Journal Irrigation and Drainage Engineering, ASCE*, 129(5), 371-375.

48. Nadesamoorthy, T. and Thomson, A. (1972). "Discussion on 'Spatially varied flow over side weirs' ", *Journal of Hydraulic Division, ASCE*, 98(12), 2234–2235.

49. Patankar, S. V. (1980). "Numerical heat transfer and fluid flow", *McGraw-Hill*, New York.

50. Patankar, S. V. and Spalding, D. B. (1972). "A calculation procedure for heat, mass and momentum transfer in three-dimensional parabolic flows", *International Journal of Heat and Mass Transfer*, 15 (10), 1787-1806.

51. Rae, Jr., W. H. and Pope, A. (1984). "Low-speed wind tunnel testing", 2nd edition, *John Wiley & Sons*, New York.

52. Rajaratnam, N. and Muralidhar, D. (1967). "Yaw and pitch probes", *Technical Report*, Department of Civil Engineering, University of Alberta, Canada.

53. Rajaratnam, N. and Muralidhar, D. (1970). "The screw-driver probe", *Journal of Hydraulic Research, IAHR*, 8(1), 65–70.

54. Rajaratnam, N. and Muralidhar, D. (1971). "Pressure and velocity distribution for sharp-crested weirs," *Journal of Hydraulic Research, IAHR*, 9(2), 241–248.

55. Ramamurthy, A. S. and Carballada, L. (1980). "Lateral weir flow model", *Journal Irrigation and Drainage Engineering, ASCE*, 106(1), 9-25.

56. Ramamurthy, A. S., Rao, V. J. and Aukle, D. A. (1985). "Free flow discharge characteristics of throatless flumes", *Journal Irrigation and Drainage Engineering, ASCE*, 111(1), 65-75.

57. Ramamurthy, A. S., Tim, U. S. and Rao, M. V. (1987). "Flow over sharp-crested weirs," *Journal Irrigation and Drainage Engineering, ASCE*, 113(2), 163-172.

58. Ramamurthy, A. S., Vo, N. D. and Balachandar, R. (1988). "Submerged flow characteristics of throatless flume", *Journal Irrigation and Drainage Engineering, ASCE*, 114(1), 185-194.

59. Ramamurthy, A. S., Vo, N. D., and Vera, G. (1992). "Momentum model of flow past weir", *Journal of Irrigation and Drainage Engineering, ASCE*, 118(9), 988-994.

60. Ramamurthy, A. S. and Vo, N. D. (1993). "Application of Dressler theory of weir flow", *Journal of Applied Mechanics, ASCE*, 60, 163-166.

61. Ramamurthy, A. S., Vo, N. D., and Balachandar, R. (1994). "A note on irrotational curvilinear flow past a weir", *Journal of Fluid Engineering*, 116, 378-381.

62. Ramamurthy, A. S., Qu, J., and Vo, D. (2006). "Nonlinear PLS method for side weir flows", *Journal Irrigation and Drainage Engineering, ASCE*, 132(5), 486-489.

63. Ranga Raju, K. G., Prasad, B., and Gupta, S. K. (1979). "Side weir in rectangular channel", *Journal of the Hydraulics Division, ASCE*, 105(5), 547-554.

64. Rhie, C. M., Chow, W. L. (1983). "A numerical study of the turbulent flow past an isolated airfoil with trailing edge separation", *AIAA Journal*, 21, 1525-1532.

65. Rouse, H. and Reid, L. (1935). "Model research on spillway crests," *Civil Engineering, ASCE*, 5(1), 10-15.

66. Rousselier, M. and Blanchet, P. (1951). "Some realizations of siphons", *ICOLD 4th Congress*, India.

67. Sananes, M. F. (1957). "Etude des seuils deversants a fente aspiratrice", *IAHR*, 7th General Meeting Transactions, Lisbon, Portugal, Vol. II, D24.1-D24.23.

68. Sarginson, E. J. (1972). "The influence of surface tension on weir flow", *Journal of Hydraulic Research*, 10, 431-446.

69. Singh, R., Manivannan, D., and Satyanarayana, T. (1994). "Discharge coefficient of rectangular side weirs", *Journal Irrigation and Drainage Engineering, ASCE*, 120(4), 814-819.

70. Sinniger, R. and Hager, W. H. (1985). "Flood control by gated spillways", 15th Congres des barrages, Commission Internationale des Grands barrages, Lausanne, Switzerland, Q.59, R.9, 121-149.

71. Skogerboe, G. V. and Hyatt, M. L. (1967). "Rectangular cutthroat flow measuring flumes", *Journal of Irrigation and Drainage Division, ASCE*, 93(4), 1-13.

72. Sotiropoulos, F. and Patel, V. C. (1995). "On the Role of Turbulence Anisotropy and Near-Wall Modeling in Predicting Complex, 3D, Shear Flows", *AIAA Journal*, 33(3), 504-514.

73. Subramanya, K. and Awasthy, S. C. (1972). "Spatially varied flow over side weirs", *Journal of the Hydraulics Division, ASCE*, 98(1), 1-10.

74. Unser, K. (1975). "Design of low head siphon spillways", *Symposium on the Design and Operation of Siphons and Siphon Spillways, BHRA Fluid Engineering*, U.K., C5.55-C5.68.

75. Uyumaz, A. and Smith, R. H. (1991). "Design procedure for flow over side weirs", *Journal of Irrigation and Drainage Engineering, ASCE*, 117(1), 79–90.

76. van Doormal, J. P. and Raithby, G. D. (1984). "Enhancements of the SIMPLE method for predicting incompressible fluid flows", *Numerical Heat Transfer*, 7 (2), 147-163.

77. Versteeg, H.K. and Malalasekera, W. (2007). "An Introduction to Computational Fluid Dynamics: The Finite Volume Method", 2nd Edition, *Pearson Education, Harlow , UK*.

78. Vischer, D. L. and Hager, W. H. (1997). "Dam Hydraulics", *John Wiley & Sons*, U.K.

79. Vo, N. D. (1992). "Characteristics of curvilinear flow past circular-crested weirs", Ph. D. Thesis, *Concordia University*, Montreal, Canada.

80. Wilcox, D. C. (2007). "Turbulence Modeling for CFD", 3rd edition, *DCW Industries, Inc.*, La Canada, California.

81. Wu, S. and Rajaratnam, N. (1996). "Submerged flow regimes of rectangular sharp-crested weirs," *Journal of Hydraulic Engineering, ASCE*, 122(7), 412-414.

82. Yakhot, V. and Smith, L. M. (1992). "The renormalization group, the ε-expansion and derivation of turbulence models", *Journal of Scientific Computing*, 7(1), 35-61.

Appendix

Tables of Data

(Some Simulation Results)

x_1, m	χ_3
0.015	0.999
0.046	0.993
0.076	0.992
0.107	0.993
0.137	0.993
0.168	0.994
0.198	0.994
0.229	0.993
0.259	0.993
0.290	0.992
0.315	0.990
0.335	0.987
0.355	0.982
0.376	0.976
0.396	0.965
0.416	0.950
0.436	0.930
0.457	0.903
0.473	0.883
0.485	0.859
0.497	0.835
0.509	0.807
0.521	0.777
0.533	0.744
0.545	0.711
0.557	0.677

x_1, m	χ_3
0.569	0.642
0.581	0.610
0.593	0.578
0.605	0.545
0.617	0.517
0.629	0.490
0.641	0.465
0.653	0.441
0.665	0.418
0.677	0.401
0.689	0.384
0.701	0.367
0.713	0.354
0.725	0.340
0.737	0.330
0.749	0.322
0.761	0.313
0.773	0.304
0.785	0.299
0.806	0.286
0.837	0.279
0.868	0.276
0.899	0.275
0.930	0.276
0.961	0.279
0.992	0.282

Table A.1) Numerical data related to

Fig. 3.2, Flume II, Test 3

x_1, m	h, m
0.015	0.185
0.046	0.184
0.076	0.184
0.107	0.184
0.137	0.184
0.168	0.184
0.198	0.184
0.229	0.184
0.259	0.183
0.290	0.182
0.313	0.179
0.328	0.177
0.343	0.173
0.359	0.167
0.374	0.160
0.390	0.150
0.405	0.138

x_1, m	h, m
0.419	0.124
0.432	0.117
0.445	0.116
0.457	0.117
0.470	0.117
0.483	0.116
0.495	0.115
0.508	0.112
0.521	0.110
0.534	0.107
0.546	0.104
0.559	0.100
0.572	0.097
0.584	0.093
0.597	0.090
0.610	0.086

Table A.2) Numerical data related to

Fig. 3.3, Flume III, Test 3

x_1, m	u_1, m/s
0.000	0.000
0.001	0.363
0.004	0.412
0.008	0.440
0.011	0.458
0.015	0.469
0.020	0.477
0.025	0.482
0.030	0.486
0.036	0.488
0.042	0.489
0.049	0.489
0.057	0.489
0.065	0.489
0.074	0.488
0.082	0.486
0.089	0.485
0.095	0.483
0.101	0.481
0.106	0.479
0.111	0.477
0.115	0.474
0.119	0.470
0.123	0.464

Table A.3) Numerical data related to

Fig. 3.4-c

x_1, m	x_3, m	x_1, m	x_3, m
-0.009	0.185	0.510	0.192
0.010	0.185	0.530	0.193
0.030	0.185	0.550	0.193
0.050	0.185	0.570	0.193
0.070	0.185	0.590	0.194
0.090	0.185	0.610	0.194
0.110	0.185	0.630	0.194
0.130	0.185	0.650	0.194
0.150	0.186	0.670	0.195
0.170	0.186	0.690	0.195
0.190	0.186	0.710	0.195
0.210	0.187	0.730	0.195
0.230	0.188	0.750	0.195
0.250	0.188	0.770	0.196
0.270	0.189	0.790	0.196
0.290	0.190	0.810	0.196
0.310	0.190	0.830	0.196
0.330	0.191	0.850	0.197
0.350	0.191	0.870	0.197
0.370	0.191	0.890	0.197
0.390	0.191	0.910	0.197
0.410	0.191	0.930	0.198
0.430	0.191	0.950	0.198
0.450	0.192	0.970	0.198
0.470	0.192	0.990	0.199
0.490	0.192	1.010	0.199

Table A.4) Numerical data related to

Fig. 4.2, Run E

x_1, m	Q, m³/s		x_1, m	Q, m³/s
-0.009	0.039		0.510	0.031
0.010	0.039		0.530	0.030
0.030	0.039		0.550	0.030
0.050	0.039		0.570	0.030
0.070	0.038		0.590	0.029
0.090	0.038		0.610	0.029
0.110	0.038		0.630	0.028
0.130	0.038		0.650	0.028
0.150	0.037		0.670	0.027
0.170	0.037		0.690	0.027
0.190	0.037		0.710	0.027
0.210	0.037		0.730	0.026
0.230	0.036		0.750	0.026
0.250	0.036		0.770	0.025
0.270	0.036		0.790	0.025
0.290	0.035		0.810	0.024
0.310	0.035		0.830	0.024
0.330	0.034		0.850	0.023
0.350	0.034		0.870	0.023
0.370	0.034		0.890	0.022
0.390	0.033		0.910	0.022
0.410	0.033		0.930	0.021
0.430	0.033		0.950	0.021
0.450	0.032		0.970	0.020
0.470	0.032		0.990	0.020
0.490	0.031		1.010	0.019

Table A.5) Numerical data related to

Fig. 4.3, Run E

x_3, m	u_1, m/s
0.000	0.000
0.002	0.179
0.005	0.263
0.008	0.330
0.011	0.380
0.014	0.416
0.017	0.440
0.020	0.455
0.023	0.464
0.026	0.469
0.029	0.471
0.032	0.471
0.035	0.469
0.038	0.465
0.041	0.457
0.044	0.439
0.047	0.429
0.050	0.423
0.053	0.416

Table A.6) Numerical data related to

Fig. 4.5, B-c

x_1, m	x_2, m	x_1, m	x_2, m
-0.155	0.155	-0.023	0.128
-0.149	0.154	-0.017	0.126
-0.143	0.153	-0.012	0.124
-0.137	0.152	-0.006	0.122
-0.131	0.151	0.000	0.120
-0.124	0.150	0.007	0.117
-0.118	0.150	0.014	0.114
-0.112	0.148	0.021	0.112
-0.106	0.147	0.027	0.109
-0.100	0.146	0.034	0.106
-0.094	0.145	0.040	0.103
-0.088	0.144	0.047	0.099
-0.082	0.143	0.053	0.096
-0.076	0.142	0.059	0.093
-0.070	0.140	0.064	0.090
-0.064	0.139	0.071	0.086
-0.058	0.138	0.076	0.083
-0.053	0.136	0.081	0.079
-0.047	0.135	0.087	0.075
-0.041	0.133	0.093	0.072
-0.035	0.131	0.097	0.068
-0.029	0.130	0.103	0.064

Table A.7) Numerical data related to

Fig. 7.2, T2

x_2, m	h, m	x_2, m	h, m	x_2, m	h, m
0.000	-0.003	0.033	0.027	0.080	0.030
0.001	-0.002	0.034	0.028	0.082	0.030
0.002	-0.001	0.036	0.029	0.084	0.029
0.003	0.001	0.037	0.029	0.087	0.028
0.004	0.002	0.039	0.030	0.089	0.027
0.006	0.003	0.041	0.030	0.091	0.026
0.007	0.005	0.042	0.031	0.094	0.026
0.008	0.006	0.044	0.031	0.096	0.025
0.009	0.008	0.046	0.032	0.099	0.023
0.010	0.009	0.048	0.032	0.101	0.022
0.012	0.011	0.049	0.032	0.104	0.021
0.013	0.012	0.051	0.033	0.107	0.020
0.014	0.013	0.053	0.033	0.109	0.019
0.015	0.015	0.055	0.033	0.112	0.018
0.017	0.016	0.057	0.033	0.114	0.016
0.018	0.017	0.059	0.033	0.117	0.015
0.019	0.018	0.061	0.033	0.119	0.013
0.021	0.019	0.063	0.033	0.122	0.012
0.022	0.021	0.065	0.033	0.125	0.010
0.024	0.022	0.067	0.033	0.128	0.009
0.025	0.023	0.069	0.032	0.130	0.007
0.026	0.024	0.071	0.032	0.133	0.005
0.028	0.025	0.073	0.032	0.136	0.003
0.029	0.025	0.075	0.031	0.139	0.002
0.031	0.026	0.077	0.031	0.142	0.000

Table A.8) Numerical data related to

Fig. 7.3-c

x_2, m	h, m	x_2, m	h, m	x_2, m	h, m
0.000	0.000	0.033	1.670	0.080	1.334
0.001	1.793	0.034	1.656	0.082	1.321
0.002	1.920	0.036	1.642	0.084	1.308
0.003	1.952	0.037	1.627	0.087	1.295
0.004	1.954	0.039	1.614	0.089	1.281
0.006	1.947	0.041	1.600	0.091	1.268
0.007	1.935	0.042	1.586	0.094	1.255
0.008	1.922	0.044	1.572	0.096	1.242
0.009	1.909	0.046	1.558	0.099	1.229
0.010	1.895	0.048	1.545	0.101	1.217
0.012	1.882	0.049	1.531	0.104	1.204
0.013	1.868	0.051	1.518	0.107	1.192
0.014	1.854	0.053	1.504	0.109	1.180
0.015	1.840	0.055	1.491	0.112	1.168
0.017	1.826	0.057	1.478	0.114	1.156
0.018	1.812	0.059	1.464	0.117	1.144
0.019	1.797	0.061	1.451	0.119	1.132
0.021	1.783	0.063	1.438	0.122	1.120
0.022	1.769	0.065	1.425	0.125	1.108
0.024	1.755	0.067	1.412	0.128	1.096
0.025	1.741	0.069	1.399	0.130	1.084
0.026	1.726	0.071	1.386	0.133	1.072
0.028	1.712	0.073	1.373	0.136	1.060
0.029	1.698	0.075	1.360	0.139	1.048
0.031	1.684	0.077	1.347	0.142	1.035

Table A.9) Numerical data related to

Fig. 7.5-c